Nanoscale

ROYAL SOCIETY OF CHEMISTRY

REVIEW

View Article Online
View Journal | View Issue

Cite this: *Nanoscale*, 2024, **16**, 1490

Nanocarbon-based sensors for the structural health monitoring of smart biocomposites

Gouri Sankar Das,[a] Vijayendra Kumar Tripathi,[b,c] Jaya Dwivedi,[c] Lokesh Kumar Jangir*[d] and Kumud Malika Tripathi *[a]

Received 31st October 2023,
Accepted 4th December 2023

DOI: 10.1039/d3nr05522a

rsc.li/nanoscale

Structural health monitoring (SHM) is a critical aspect of ensuring the safety and durability of smart biocomposite materials used as multifunctional materials. Smart biocomposites are composed of renewable or biodegradable materials and have emerged as eco-friendly alternatives of traditional non-biodegradable glass fiber-based composite materials. Although biocomposites exhibit fascinating properties and many desirable traits, real-time and early stage SHM is the most challenging issue to enable their long-term use. Smart biocomposites are integrated with sensors for *in situ* identification of the progress of damage and composite failure. The sensitivity of such smart biocomposites is a key functionality, which can be tuned by the introduction of an appropriate filler. In particular, nanocarbons hold promising potential to be incorporated in SHM applications of biocomposites. This review focused on the potential applications of nanocarbons in SHM of biocomposites. The aspects related to fabrication techniques and working mechanism of sensors are comprehensively discussed. Furthermore, their unique mechanical and electrical properties and sustainable nature ensure seamless integration into biocomposites, allowing for real-time monitoring without compromising the material's properties. These sensors offer multi-parameter sensing capabilities, such as strain, pressure, humidity, temperature, and chemical exposure, allowing a comprehensive assessment of biocomposite health. Additionally, their durability and longevity in harsh conditions, along with wireless connectivity options, provide cost-effective and sustainable SHM solutions. As research in this field advances, ongoing efforts seek to enhance the sensitivity and selectivity of these sensors, optimizing their performance for real-world applications. This review highlights the significant advances, ongoing efforts to enhance the sensitivity and selectivity, and performance optimization of nanocarbon-based sensors along with their working mechanism in the field of SHM for smart biocomposites. The key challenges and future research perspectives facing the conversion of nanocarbons to smart biocomposites are also displayed.

1. Introduction

The advent of smart biocomposites offers a synergy of sustainable biobased materials and advanced composite technologies in the field of materials science.[1] This novel category of materials are composed of biodegradable polymers or natural fibers, resulting in an innovative material possessing mechanical characteristics akin to those of conventional glass fiber-based composite materials.[2] These eco-friendly, lightweight, and sustainable materials hold the promise of revolution of various industries, such as aerospace,[7] construction and building material,[6] oil and gas industry,[227] marine and shipbuilding,[8] electrochemical,[5] textile and apparel manufacturing, electronics,[3] and pharmaceuticals.[4] Although smart biocomposites hold significant achievements, the prediction of their deformation mechanism remains a challenge because they may damage differently by compressive or tensile strain unlike metals or traditional composites.[9] In general, 'damage' is characterized as a substantial factor that affects the structural behaviour, leading to a decline in the present or future performance of a structure. Consequently, a precise explanation of damage involves a comparison between two distinct states of a structure: one in a state of 'health' and the other in a state of 'damage'.[10] In definitional terms, a healthy structure operates excellently and maintains its integrity over its lifespan.[11] Conversely, within the realm of structural identification,

[a]*Department of Chemistry, Indian Institute of Petroleum and Energy, Visakhapatnam, Andhra Pradesh, 530003, India. E-mail: kumud@20010@gmail.com*
[b]*Department of Chemistry, Banasthali Vidyapith, Banasthali, Rajasthan-304022, India*
[c]*Department of Chemical Engineering, Indian Institute of Technology Kanpur, Kanpur, 208016 UP, India*
[d]*Department of Chemistry, Indian Institute of Technology BHU, Varanasi-221005, India. E-mail: lokesh7785@gmail.com*

damage is linked to alterations initially in the material and subsequently in the geometry and topology of the structure, which includes modifications of the boundary conditions.[12] Current methods for detecting damage span a broad spectrum, ranging from traditional inspection methods performed by experts to advanced automated approaches employing smart sensors and artificial intelligence. The latter identification process combines science and engineering, forming the basis of the interdisciplinary field known as structural health monitoring (SHM). The SHM of smart biocomposites utilised in critical infrastructure like bridges, buildings, and dams is critical for ensuring safety from catastrophic consequences.[13,14] SHM allows the early detection of structural issues before they reach critical problems.[15] This proactive approach can not only extend the lifespan of biocomposites but also reduce the cost and disruption associated with major repairs. In addition, SHM can also contribute to sustainability in terms of energy saving and waste reduction. Furthermore, SHM can provide real time information of structural health at extreme events or natural disasters.[16,17] The main objective of the SHM system is to establish a real time health monitoring network for the future advancement of smart biocomposites.

In this regard, various SHM techniques have been utilized such as non-destructive evaluation,[18,19] self-sensing material system,[20–22] and smart embedded sensor.[23–25] The non-destructive testing methods are generally utilised in the last step of the major process, and the structure size limits the application.[26] Additionally, self-sensing materials system may have a limited sensing range, which can make it challenging to monitor complex structures.[20] On the other hand, incorporating integral sensing systems within the composite structure enhances the ability of real time SHM during the manufacturing process by effectively monitoring crucial parameters like strain or temperature variations. Furthermore, the integration of sensors within the structure provides protection from the operational environment, ultimately extending the lifespan of the sensors.[27] Additionally, this method offers a cost-efficient solution, increasing the durability of smart biocomposites by enabling continuous data collection for timely repairs and maintenance, hence reducing the need for unnecessary maintenance procedures.[28]

Commercially available strain sensors exhibited the limitations of poorer sensing within a few percentages owing to the inadequate stretchability of metal and semiconductors.[29,30] Strain sensors with high sensing efficiency (>50%) are of particular interest for the fabrication of interactive election devices to be human-friendly. The ability or performance of these sensors are measured by gauge factor, durability, stability, response time, sensing range, and the correlation between strain and relative resistance change. Various types of strain or pressure sensors including, strain gauges, fiber optic, piezoresistive,[31] piezoelectric,[33] Raman pressure sensor,[34] field effect transistor,[35] and capacitive sensors[32] are used in SHM to assess the condition and performance of structures. These sensors are fabricated using diverse functional nanomaterials such as MXene/AgNW composite,[36] PEDOT:PSS fibers,[37] MXene/PEDOT:PSS@Melamine foam,[38] ZnO/PVDF composite,[39] metal nanoparticles, and metal organic framework depending on their working mechanism.[40–45] Among these nanomaterials, nanocarbons such as carbon black (CB), carbon nanotubes (CNTs), carbon nanoonions (CNOs), and graphene are often considered superior to other nanomaterials for strain sensors because of the combination of their exceptional properties and performance advantages. Nanocarbons exhibits high sensitivity,[49] exceptional mechanical properties,[46] high electrical conductivity,[48] wide strain range,[51] high chemical stability,[53] lightweight,[52] high thermal stability,[47] high signal-to-noise ratios,[228] electrochemical charge storage capicity[54] and multi-directional sensing,[50] which make them suitable for a wide range of applications. The nanocarbons can be easily incorporated in different polymer matrixes to form stretchable and mechanically stable strain sensors. Nanocarbon-based sensors exhibit ultra-sensitivity, stability, and responsiveness to environmental factors that makes them

Gouri Sankar Das

Gouri Sankar Das received his BSc degree in Chemistry (Honours) from Burdwan Raj College, West Bengal, India and MSc degree in Chemistry from the University of Burdwan, India. He is currently a PhD student at the Chemistry Department, Indian Institute of Petroleum and Energy, Visakhapatnam, India. He has been doing his research work under the supervision of Dr. Kumud Malika Tripathi. His research work is focused on the synthesis of green nanocarbons for renewable energy applications.

Vijayendra Kumar Tripathi

Vijayendra Kumar Tripathi received his BSc degree in Chemistry from Christ Church College, Kanpur, India and MSc degree in Chemistry from DAV College, Kanpur, India. He is currently a PhD student at the Chemistry Department, Banasthali Vidyapith, Rajasthan, India. He has been doing his research work under the supervision of Dr. Jaya Dwivedi. His research work is focused on the synthesis of green nanocarbons for environmental remediation applications.

suitable for monitoring the structural integrity of biocomposite materials. Nonetheless, the development process is complex because of their small size and structure, which can cause difficulty in uniform incorporation and structural assembly in the polymer matrix.[55] Recent research reports have highlighted the successful development of nanocarbons using various techniques to enhance the strain-sensing capabilities.[56] These assembly methods encompass approaches like uniform blending[57] and structured arrangements[58] such as micro yarns,[59] nanofibers,[60] foams,[61] and nanofiber membranes.[62] The characteristics of these strain sensors are changed with the specific assembly method employed. Although the sensors fabricated directly using nanocarbons show higher strain sensitivity than the nanocarbon-based composites but the use of these polymer substrates enhance the linear response, expand the strain range, and improve the stability.[63] The enduring interactions between carbon nanomaterials and polymers are pivotal for optimal sensing performance. For example, the incorporation of CNTs in the matrix of polyaniline (PANI) enhances the flexibility and range of sensitivity of conductive yarn strain sensors.[64] In addition, the piezoresistive sensing performance of the pressure sensor can be improved by the incorporation of cellulose nanocrystal in the CNTs/waterborne polyurethane (WPU) composite.[65] Apart from the polymer, the sensitivity of elastic rubber-based flexible strain sensor can be achieved with low detection limit, wide detection range, and high gauge factor by decorating the dual conducting layer of CNT and reduced graphene oxide (rGO) on elastic rubber band.[66] Moreover, the introduction of CNTs in the conducting layer of Ag nanoparticles on spandex fiber improves the range of sensitivity as well as the response/recovery time of wearable strain sensor.[67]

Nanocarbons derived from biomass may have a lower carbon footprint compared to traditional carbon sources and it indirectly contributes to carbon sequestration.[68] These materials may be cost-effective, eco-friendly, and biodegradable, offering environment-friendly end-of-life disposal options, especially in applications where degradation over time is acceptable.[69] In addition, the production methods may have lower energy requirements compared to traditional methods, contributing to reduced environmental impact.[70–73] Sustainable nanocarbons can be easily tailored based on the specific features of the biomass source, providing a precise control over the material's properties.[74–76]

This review article presents the latest progress of the burgeoning field of nanocarbon-based sensors and their transformative impact on the SHM of smart biocomposites. The utilization of nanocarbons in SHM, encompassing various sensor types, and delving into the role of nanocarbons in electronic skin applications are discussed in detail. Furthermore, the review provides a detailed exploration of different types of nanocarbon-based sensors, elucidating their operational mechanisms. In closing, conclusions and insights into the future prospects of these sensors, illuminating their potential to revolutionize how to monitor and uphold the integrity of advanced composite structures in various sectors have been discussed. The insights within this review serve as a valuable resource for research scholars, scientists, and industries engaged in the field of strain sensors and SHM of biocomposite materials.

2. *In situ* structural health monitoring

SHM refers to the process of continuously monitoring the integrity and condition of a structure over time. Various sensors involve monitoring the performance, strain, crack, and other critical factors affecting the structural integrity of aircraft, buildings, bridges, dams, and other engineered structures.[77] These sensors continuously collect data on factors such as vibrations, temperature, humidity, strain, and deformation; structural health can be accessed by analyzing them. SHM is important in various industries such as civil engineering, aerospace, energy, medical, and transportation as it helps

Jaya Dwivedi

Dr. Jaya Dwivedi is working as Professor and Head, Department of Chemistry and Dean, School of Life Sciences at Banasthali Vidyapith, Rajasthan. Her area of specialization is organic synthesis, material development, and natural products. She has published several articles in highly reputed national and interational journals. Besides, she has also authored a few book chapters with renowned publishing houses.

Lokesh Kumar Jangir

Dr. Lokesh Kumar Jangir earned his PhD in Physics from MNIT Jaipur (2018), MTech degree in Computer Science and Data Processing from IIT Kharagpur (2012), MSc in Physics from the University of Rajasthan (2009), and BSc from the University of Rajasthan (2006). He is currently working as a post-doctoral fellow at IIT BHU, Varanasi. His research interests focus on nanomaterials for optoelectronics, block copolymer nanotemplates, and carbon nanostructure for energy applications.

prevent catastrophic failures, ensures safety, reduces maintenance costs, and enhances the overall performance and reliability of critical infrastructure and assets.[78,79] *In situ* SHM is a crucial aspect of securing the structural or operational safety of smart biocomposite materials in real-world applications. Traditional SHM methods often rely on external sensors or periodic monitoring, which may not be reliable for the continuous inspection of biocomposites used in dynamic and remote environments. *In situ* SHM for smart biocomposites often include the use of embedded actuators and sensors. Nanocarbon-based sensors offer a compelling solution for *in situ* SHM of smart biocomposite by strain sensing, damage detection, and pressure monitoring.[80]

2.1 Strain sensing

The measurement of strain within smart biocomposites is one of the critical parameters in real time and long term SHM. Strain sensing using nanocarbon-based sensors provides valuable insights into the material's mechanical behaviour and its response to external loads and environmental conditions. Among various strain sensing materials, nanocarbon-based sensors, including CNTs and graphene, exhibit outstanding sensitivity to strain due to their unique electrical, mechanical, and optical properties.[81–83] Furthermore, the band gap of carbon-based materials can be opened under strain due to the breaking of sublattice symmetry, which make them promising materials for strain sensing.[84] Three dimensionally (3D) interconnected vertically-aligned CNT are being utilized as sensory films in resistive strain sensors.[85–87] These sensors can be fabricated using several techniques. For instances, vertically-aligned CNT can be directly embedded in the polymer matrix or directly laid on to the polymer substrate *via* the dry-spinning technique, or CNT films can grow on a catalyst with a patterned layout by carefully selecting and manually transferring onto polymer substrates.[85,87,88] The strain-sensing capability of CNT-based sensors relies on alterations in the structure when subjected to strain. The CNT layers become less tightly packed on stretching, which causes a reduction in contact between neighbouring CNTs proportionate to the applied strain. As a result, the electrical resistance of the sensors increases. This process occurs gradually due to the intricate entanglement of the CNT films' morphology. Consequently, these devices typically show linear sensitivity across a wide range of strains, extending to several hundred percent.[87–89] An exceptionally effective metal flexion sensor can be achieved by incorporating a super-aligned CNT sheet between an elastomer substrate and a metallic sensing film, which expressively improves the sensor's linearity of response, all the while maintaining a high level of sensitivity.[89] Additionally, highly linear piezoresistive strain sensor can be develop by single-walled CNTs encapsulated in a nonfluorinated super hydrophobic coating, providing water resistance during elastic deformation, even at 100% strain.[90] In contrast to CNT, graphene offers advantage in scalable device production using top-down approaches, which aligns with the existing semiconductor manufacturing processes.

Strain causes shift in the electronic band structure of graphene, leading to an attractive change in its electrical properties and electromagnetic coupling. Moreover, several theoretical studies on strained graphene show that under asymmetrical strain distribution, the Fermi velocity is reduced and the Dirac cones are shifted, which introduces a pseudomagnetic field and can be used to engineer the electronic structure.[91] Even though the strain can cause additional scattering and resistance decrease,[92] different methods have been adopted for the fabrication of graphene-based strain sensors such as layer-by-layer (LBL) deposition and chemical vapour deposition (CVD). Graphene woven fabrics (GWFs) strain sensor was developed by the CVD method to monitor real time various strain levels of human motion signals. On applying stress, cracks density within the network increases, causing a reduction in the available current pathways and an increase in resistance. In order to mould around human skin well to ensure the response of real signals, a new kind of electronic skin was developed with graphene woven fabrics, polydimethylsiloxane, and medical tape.[93] However, CVD-grown graphene-based sensors involve expensive and complicated process, which is not appropriate for practical applications. To overcome this problem, Wang *et al.* fabricated highly stretchable, sensitive, wearable graphene strain sensors using the LBL deposition technique, as illustrated in Fig. 1.[94]

Stretchable yarns such as rubber (RY), nylon covered rubber (NCRY), and wool yarns (WY) were used to develop the strain sensor because they can be utilised for wearable fabric. The sensing performance of the sensors is demonstrated in Fig. 2.[94] The RY sensor is placed within the PDMS layer on an

Kumud Malika Tripathi

Dr. Kumud Malika Tripathi is a Ramalingaswami Faculty/ Assistant Professor at the Department of Chemistry, Indian Institute of Petroleum and Energy, Visakhapatnam, India. She earned her PhD in Chemistry from the Indian Institute of Technology, Kanpur, in 2013. Before joining IIPE, she held several positions, including Assistant Professor at Gachon University, South Korea, postdoctoral fellow at the University of South Brittany, Lorient, France, and IIT Kanpur, India. Her research activities include the green synthesis of multifunctional nanomaterials for energy, healthcare, and environmental applications. She works at the interface of chemistry, materials science, and biology, exploring new nanomaterial-based strategies for environmental monitoring and remediation, self-recharge power units, energy storage devices, CO_2 capture and conversion, flexible electronics, and photocatalytic water splitting for green hydrogen production.

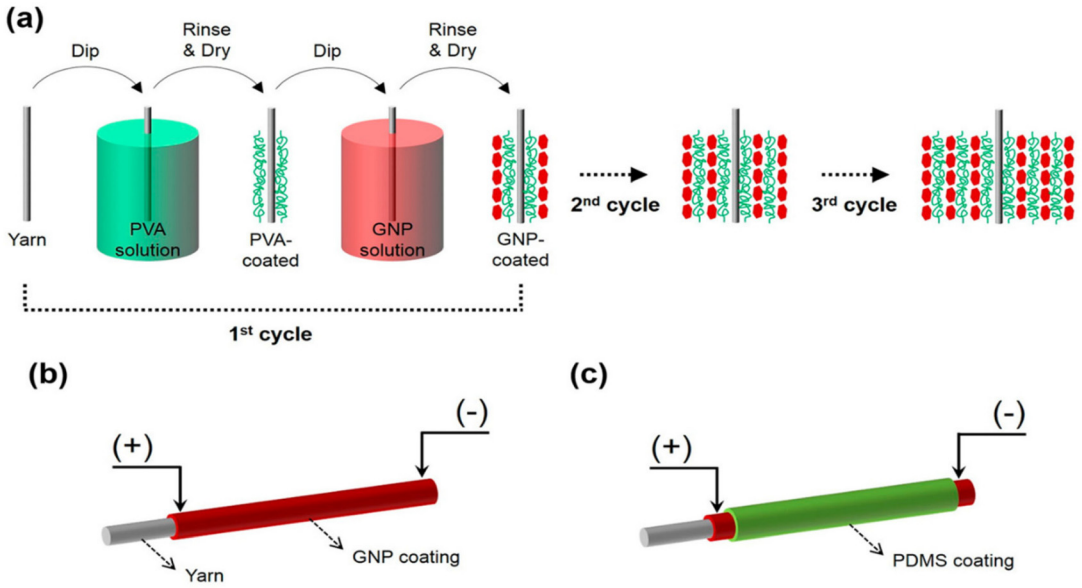

Fig. 1 (a) Steps in the LBL process for the fabrication of a graphene strain sensor using a stretchable yarn, (b) without and (c) with PDMS coating. Reproduced with permission.[94] Copyright 2015 American Chemical Society.

elastomeric medical patch (as shown in Fig. 2a), and the patch is affixed onto the throat (Fig. 2b). The bending and stretching of elastomeric patch are displayed in Fig. 2c and d, which is able to generate stress for the sensor. Fig. 2e shows a relative change in resistance of the sensor when the tester spoke several words since every individual word led to distinct movements of the laryngeal prominence. The NCRY sensor-based elbow wrap (Fig. 2f) is used to monitor the largescale motion like elbow bending at the angles of 45°, 90°, and 135°, as demonstrated in Fig. 2g, h, and i, respectively. The relative change in resistance increases with larger banding motions (Fig. 2j), indicating the sensors ability to detect and quantify the applied strain. In order to compare the piezoresistive response of WY and NCRY sensors, a data glove is used with index and middle fingers made by the WY and NCRY sensors, respectively (Fig. 2k, l, and m). The opposite response of increment and decrement in resistance for the similar bending of the WY and NCRY sensors were observed under strain (Fig. 2n), which can be advantageous for identifying the sensor that produces the signal.[94] Moreover, the fabrication of graphene composite materials based upon polymers has attracted considerable amount of interest to provide the route for a new type of materials with enhanced performance and new functionality.[95] Graphene has the ability to be easily dispersed in diverse polymer matrices. Polymer–graphene composites encountered outstanding properties for novel technological applications due to the molecular level dispersion of graphene in the polymer matrix and provided high interface between graphene and polymer.[96] The hybrid structures of CNT and graphene may enhance the overall strain sensitivity of sensors. The *in situ* crosslinking of PDMS in the hybrid structure of CNT/rGO showed improved sensitivity as compared to the CNT/PDMS-based strain sensor.[97] Additionally, 3D rGO foam and natural rubber-based flexible strain sensor was able to detect human motion.[98] Overall, nanocarbons have advantages in *in situ* SHM. However, uniform dispersion, reproducibility, and long-term stability challenges are need to be addressed for widespread implementation.

2.2 Damage detection

In situ damage detection by monitoring resistance change under strain of the biocomposite to identify damage or structural changes without need for the interruption of its operation. Piezoresistive strain sensors are integrated within the structure to continuously monitor strain levels, and any deviation from expected values can indicate damage or structural issues. This technique is mostly applicable for carbon fiber-based composites because of their high conductivity.[99,100] Furthermore, the composite with low conductivity does not respond to these sensors. To address this limitation, the enhancement of the structure's electrical conductivity and self-sensing capabilities was achieved through the incorporation of nanocarbon-based fillers such as CB, CNTs, carbon nanofibers, and graphene.[101] In this regard, Tripathi *et al.* fabricated quantum resistive sensors (sQRS) *in situ* on the flax fibers/epoxy matrix interface using spray sensing LBL process for monitoring deformation as well as damage of the smart biocomposite.[102] The sensing layer was developed by dissolving CNTs into an epoxy solution in chloroform, as displayed systematically in Fig. 3a. Sensors 1 and 2 were embedded symmetrically, as shown in Fig. 3a, to monitor the difference between elasticity and inelasticity of flax fibers/epoxy composite. The initial resistance of both sensors is different for the same flax fiber content, and their gauge factor is nearly the

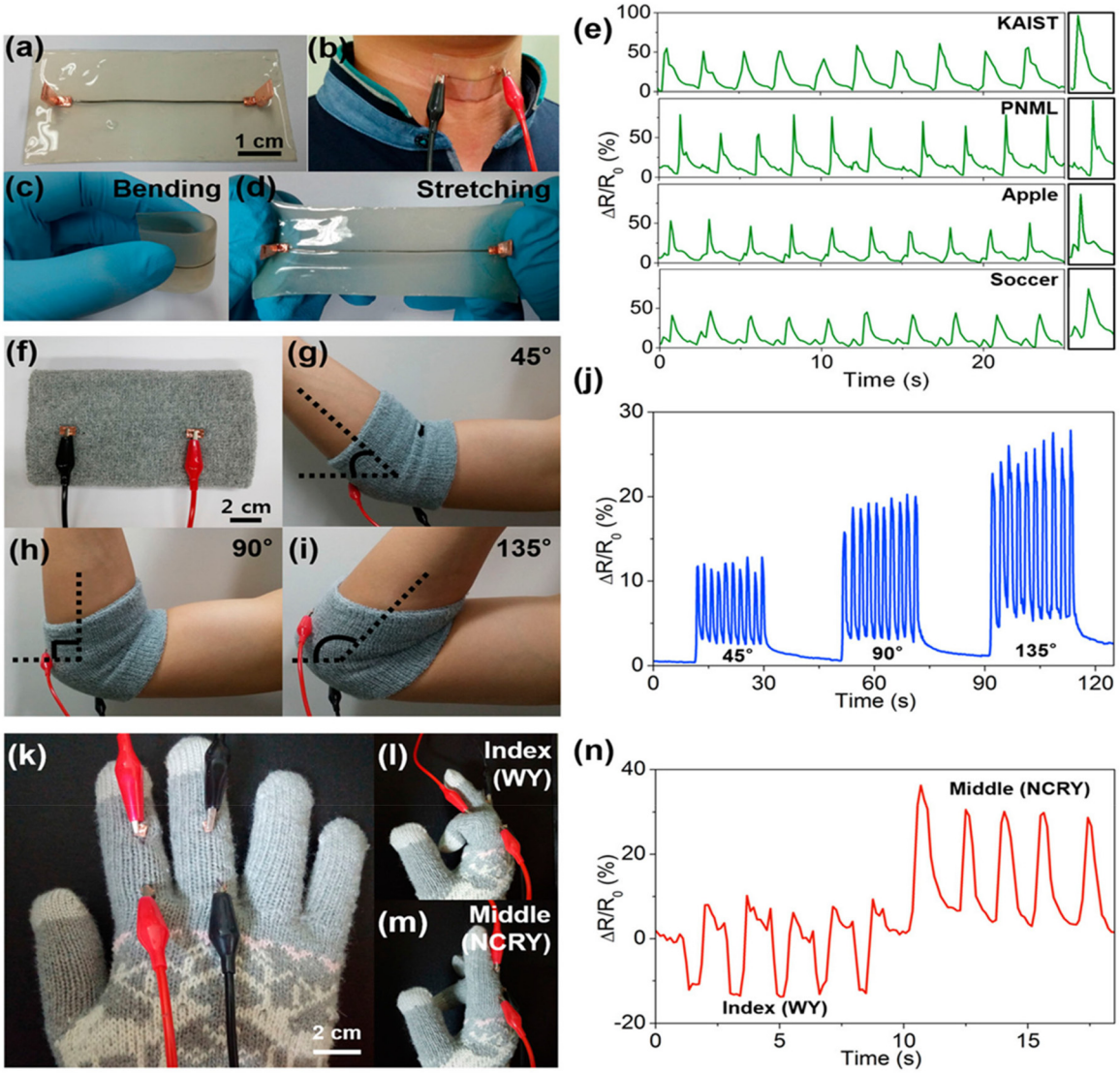

Fig. 2 (a–d) Photographs showing the RY strain sensor embedded in an elastomeric patch that is bendable and stretchable for the detection of the small-scale motions of the throat. (e) Relative resistance changes of the RY strain sensor associated with muscle motions for different phonations. (f–i) Photographs showing the NCRY strain sensor sewn in an elbow wrap to monitor the bending motion of the arm at different angles of 45°, 90°, and 135°. (j) Relative resistance changes for the NCRY strain sensor according to the bending motions. (k–m) Photographs showing the WY and NCRY sensors implanted in a glove for recording the movements of the index and middle fingers. (n) Relative resistance change of the sensors, showing distinct signals. Reproduced with permission.[94] Copyright 2015 American Chemical Society.

same for the initial two cycles. The small signal curvature changes from the third cycle due an inflection and it becomes clearly visible in the last cycle that leads to breakage (Fig. 3b). In this way, sQRS are able to detect the damage of the biocomposite before its complete failure.[102] Furthermore, onion-like nanocarbon can also be utilized in place of CNTs to create a conductive network in the polymer matrix. In this regard, Chowdhury *et al.* designed QRS by dispersing diesel engine pollutant waste-derived onion-like nanocarbon in poly(lactic acid) (PLA) matrix. These sensors were embedded on the surface of flax fiber to fabricate flax fibers–PLA biocomposite plate using spray LBL deposition, as illustrated in Fig. 3c. The prepared QRS showed the deformation of the composite material leading up to its ultimate failure. The different kinds of linear mechanical deformation in relative change in resistance response (Fig. 3d) strain range up to 0.2% and 0.2–2.5% can be understood by loading/unloading cycle test below elastic limit and above elastic limit. Fig. 3e represents the loading/unloading cycle test below 0.2% strain showing the elastic nature of fibers–PLA biocomposite because of the reproducibility of relative resistance change. Nevertheless, the relative resistance change does not reach its initial value as the strain increases from 0.1 to 0.5% (Fig. 3f), which represents irreversible behaviour due to the viscoelastic nature of the biocomposite. The relative resistance change curve (Fig. 3f) tends to be linear for the first two cycles. However, after the second

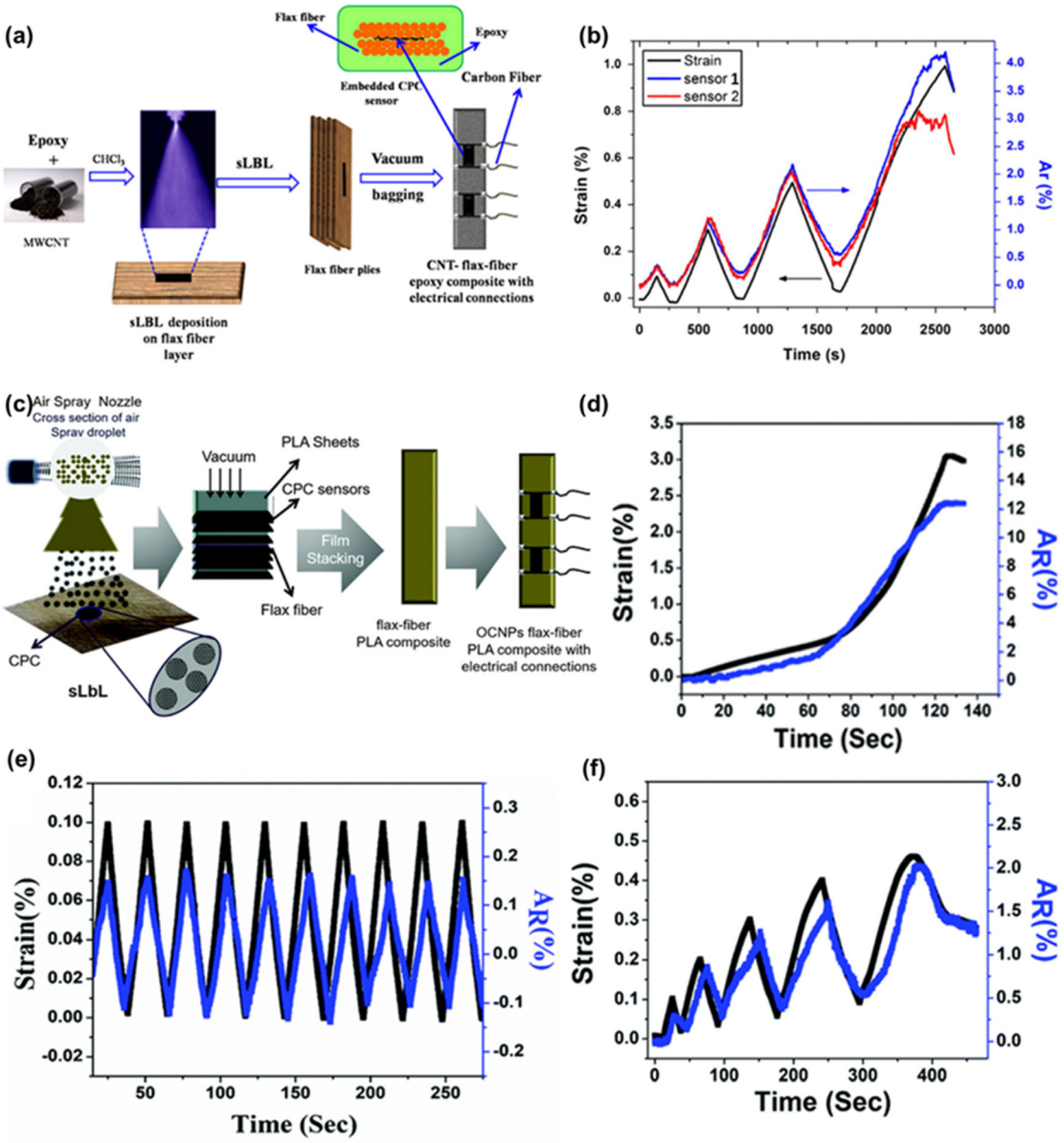

Fig. 3 (a) Schematic illustration of fabrication steps and structure quantum resistive sensor instrumented flax fibers/poly(epoxy) biocomposites. (b) Incremental loading/unloading cycling under and over the elastic limit monitored by sensors 1 and 2. Reproduced with permission.[102] (c) Schematic illustration of the spray layer-by-layer fabrication of sensors on the flax fiber surface and the fabrication of flax fibers–PLA biocomposite plate with embedded QRS sensor. Variability and trends in the electrical resistance (blue line) of the onion like nanocarbons–flax fiber–PLA composite with applied strain (black line) over time. (d) Linear increase in the relative resistance change with the static tensile strain until fracture, (e) during cyclic loading and unloading, (f) during cycling with incrementally increasing strain. Reproduced with permission. Reproduced with permission.[103] Copyright The Royal Society of Chemistry and the Centre National de la Recherche Scientifique 2021.

cycle, non-linearity becomes more pronounced, signifying the occurrence of initial microcracking at the biocomposite interface, eventually leading to complete failure.[103] Furthermore, the *in situ* growth of CNTs in cement-based materials was utilised for the early detection of damage in the structure. Fly ash (FA) was utilized for the uniform dispersion of CNTs in the cement-based structure. The gauge factor of FA-coated CNT 2.0 wt% CNT concentration was found to be 6544.[104] In addition, the hybrid structure of CNT and graphene-based film sensor was utilized for out-of-plane shear damage detection of epoxy composites.[105] It is important to develop scalable manufacturing processes with long-term stability and uniform dispersion of nanocarbon materials for *in situ* damage detection of smart biocomposites.

2.3 Pressure monitoring

Pressure monitoring involves measuring and tracking the force per unit area exerted by a fluid, gas, or mechanical system on a

surface or within a confined space.[106] The pressure sensors are utilized in the touch panels, human motion monitoring, and real-time SHM of the smart biocomposite. Based on the working mechanism, pressure sensors are generally divided into four categories such as piezo-resistivity,[107] triboelectricity,[108] capacitive,[109] and piezoelectricity.[110] The piezoresistive pressure sensor converts mechanical pressure into resistance change. It has cost-effective synthesis, simple design, scalability, and fast response. The properties and performance of sensing devices depends on substrate and active layers, which are optimized through structure redesign and raw material selection. From the view point of human health monitoring, piezoelectric pressure sensors require high sensitivity, high mechanical flexibility, and wide linear range.[55] The piezoresistive pressure sensors are optimized by the active layer and surface and bulk structure of the substrate. To achieve ultrahigh sensitivity, each layer should be rough or uneven surface so that small amounts of applied pressure may cause obvious change in the resistance because of rough contact between the active layers and electrodes.[111] Furthermore, for large pressure measurement ranges, the active layer requires continuous variation of resistance. For this purpose, the selection of a suitable conducting material is also an important aspect for the fabrication of high-performance flexible sensors.

Most sensors use metal-based nanomaterials as a conductive filler.[112] However, nanocarbon-based hybrid-conducting material with high aspect ratio of one-dimensional material combined with two-dimensional material shows high performance as compared to solely metal nanowires because of the synergistic effect.[113,114] In order to achieve this, Li *et al.* fabricated a flexible pressure sensor with a hierarchical nanonetwork of silver nanowires, graphene, and polyamide nanofibers (Ag NWs/GR/PANF). The schematic representation of the pressure sensing model is demonstrated in Fig. 4a.[115] Without pressure, the layers of sensors are far from each other; therefore, there is no conductive path between the active layer and electrodes. However, when external pressure is applied, electrodes move close to the active layer (Ag NWs/GR/PANF film), an electrically conducting path established between them. As the pressure increases more, the conductive pathways increase because at high pressure, bulk resistance plays a dominant role rather than contact resistance in overall resistance change, after unloading the sensor returns to their initial stage. Fig. 4b shows that current changes linearly with voltage at different pressures, which is consistent with the above mechanism. The change in current ($\Delta I/I_0$) as a function of applied pressure is illustrated in Fig. 4c, which is also incorporated with the above explained mechanism. The pressure sensor offers rapid response and relaxation time (<20 ms), as depicted in Fig. 4d. The Ag NWs/GR/PANF skin sensors show excellent performance in real-time biomedical monitoring and clinical diagnosis. To monitor muscle movement, a highly flexible sensor is attached to the neck (Fig. 4e) of a person. Fig. 4f and g illustrate higher sensitivity when the speaker said some sentences and words. The current *versus* time curve also demonstrates the same response when the speaker said some words. Additionally, the skin sensor was also utilized for the pulse signal monitoring; for this purpose, a skin sensor is attached on the wrist (Fig. 4h) of a person to monitor the pulse period and waveform in real time. Fig. 4i demonstrates a female pulse signal, and the pulse rate was found to be 73 beats per minute. Moreover, Fig. 4j shows that each pulse waveform has three characteristic peaks corresponding to percussion (P), tidal (T), and diastolic waves (D).[115]

Graphene and CNT-based hybrid structures were also utilized for a wide range of pressure monitoring with high sensitivity. The sensor was prepared by a PDMS composite sponge incorporated with rGO/CNT filler *via* polydopamine. The stability of the sensor was tested by 500 loading–unloading cycles. In addition, the gauge factor of the sensor was found to be 2.13.[116] Utilizing *in situ* transmission electron microscopy observation techniques, it is possible to manipulate a graphene layer at the atomic scale, achieving nanoscale sliding. Based on this technique a pressure sensor was fabricated, which demonstrated a high gauge factor of 4303 at maximum strain of 93.3%, low hysteresis, and high stability. Therefore, the sensor can be utilized for the SHM of the biocomposite.[117]

3. Application of nanocarbons in structural health monitoring

Nanocarbons are utilized as various sensing components in multifunctional SHM devices because of their excellent properties such electrical conductivity, low toxicity, high thermal stability, high chemical stability, and availability of various functional groups for modification.[118–120] Furthermore, nanocarbon-based device shows extra ordinary features such as easy fabrication, low power consumption, easy miniaturization, and bulk production.[121–124] Herein, we discuss the utilization of nanocarbon-based material in SHM *via* different techniques including piezoresistive sensors, Raman analysis, optical sensors, and field-effect transistor.

3.1 Piezoresistive sensors

A piezoresistive sensor transforms the electrical resistance of a system into an electrical signal in response to mechanical stimuli. Nanocarbon-based piezoresistive sensor is greatly needed for SHM because of its easy signal processing and simple fabrication. The performance of these sensors effectively depends on the selection of nanocarbons and microstructure of the sensor.[125,126] For example, Hu *et al.* designed a carbon black (CB)-coated polydimethylsiloxane (PDMS) piezoresistive-type flexible sensor, which showed higher conductivity than those of polymer composites filled with CB.[127] Furthermore, the concentration of CB in the polymer matrix may tune the conductivity of the sensor. In this regard, an electrode free piezoresistive sensor was developed using CB as a conducting material and polyvinylidene fluoride–hexafluoropropylene (PVDF–HFP) as the polymer matrix. CB particles function as inner electrodes as well as the piezoelectric enhancer. The schematic diagram of the prepared sensor is shown in

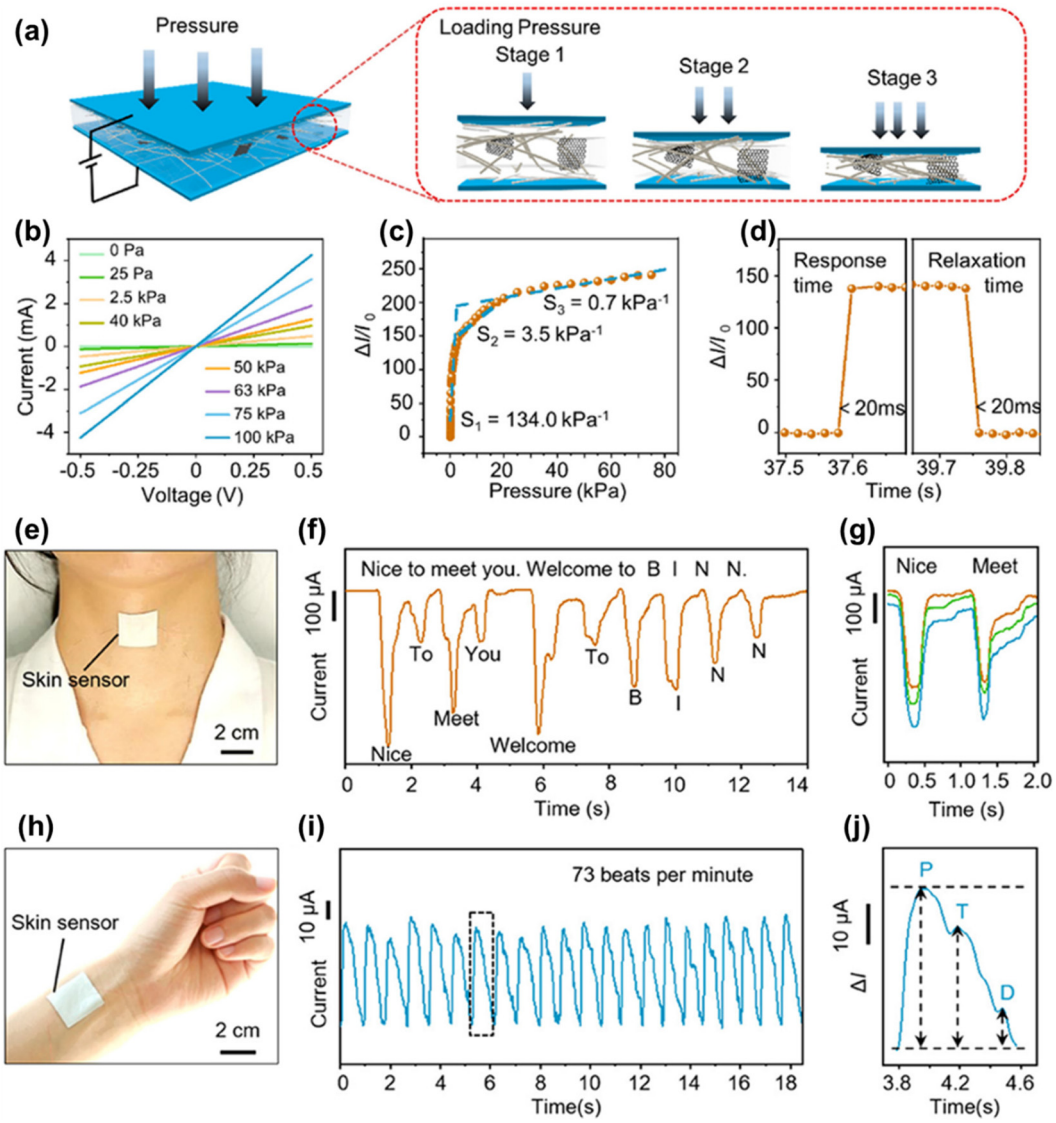

Fig. 4 (a) Schematic illustration of the mechanism of the Ag NWs/GR/PANF pressure sensor. (b) *I*–*V* curves of the device under different applied pressures. (c) Current response ($\Delta I/I_0$) *vs.* applied pressure. (d) A response and relaxation time within 20 ms. (e) Photograph of pressure sensor attached to the throat. (f) Responsive curves when wearer spoke "Nice to meet you. Welcome to BINN". (g) Real-time current signal responding to different words. (h) Photograph of device loaded on the wrist for testing a wrist signal. (i) Original current signals for monitoring wrist pulses of a healthy person. (j) A single pulse signal that contains characteristic peaks called P-wave, T-wave, and D-wave. Reproduced with permission.[115] Copyright 2020 American Chemical Society.

Fig. 5a.[128] As depicted in Fig. 5b, the sensor was utilized in two sensing modes: in mode 1 the impacted area of sensor is fully covered by copper foil, whereas in mode 2, it is not fully covered by copper foil. In mode 2, the copper foil did not work as electrodes; it was just as if a wire is connected with another copper wire; therefore, this mode was named as "electrode free". The porous PVDF–HFP film showed higher response as compared to non-porous PVDF–HFP film without the incorporation of CB nanoparticles, as demonstrated in the orange part of Fig. 5c. Additionally, the flexibility and sensitivity of the film was affected because of the low mechanical strength of copper in mode 1. Therefore, mode 2 was utilized for porous PVDF–HFP film with different concentrations of CB nanoparticles (blue part of Fig. 5c). The incorporation of CB nanoparticles in PVDF–HFP matrix significantly enhance the performance of the sensor, especially at 5 wt% of CB nanoparticles in porous PVDF–HFP matrix.[128] The significant improvement in piezoresistive behaviour was observed in the composite of CB with the PVDF matrix with the addition of either poly(butylene succinate) (PBS) or poly(methyl methacrylate) (PMMA) in the PVDF matrix.[129]

Apart from CB, CNT is also a promising material for flexible electronics because of its excellent electromechanical property.[130] To utilize this property, He *et al.* designed a single-

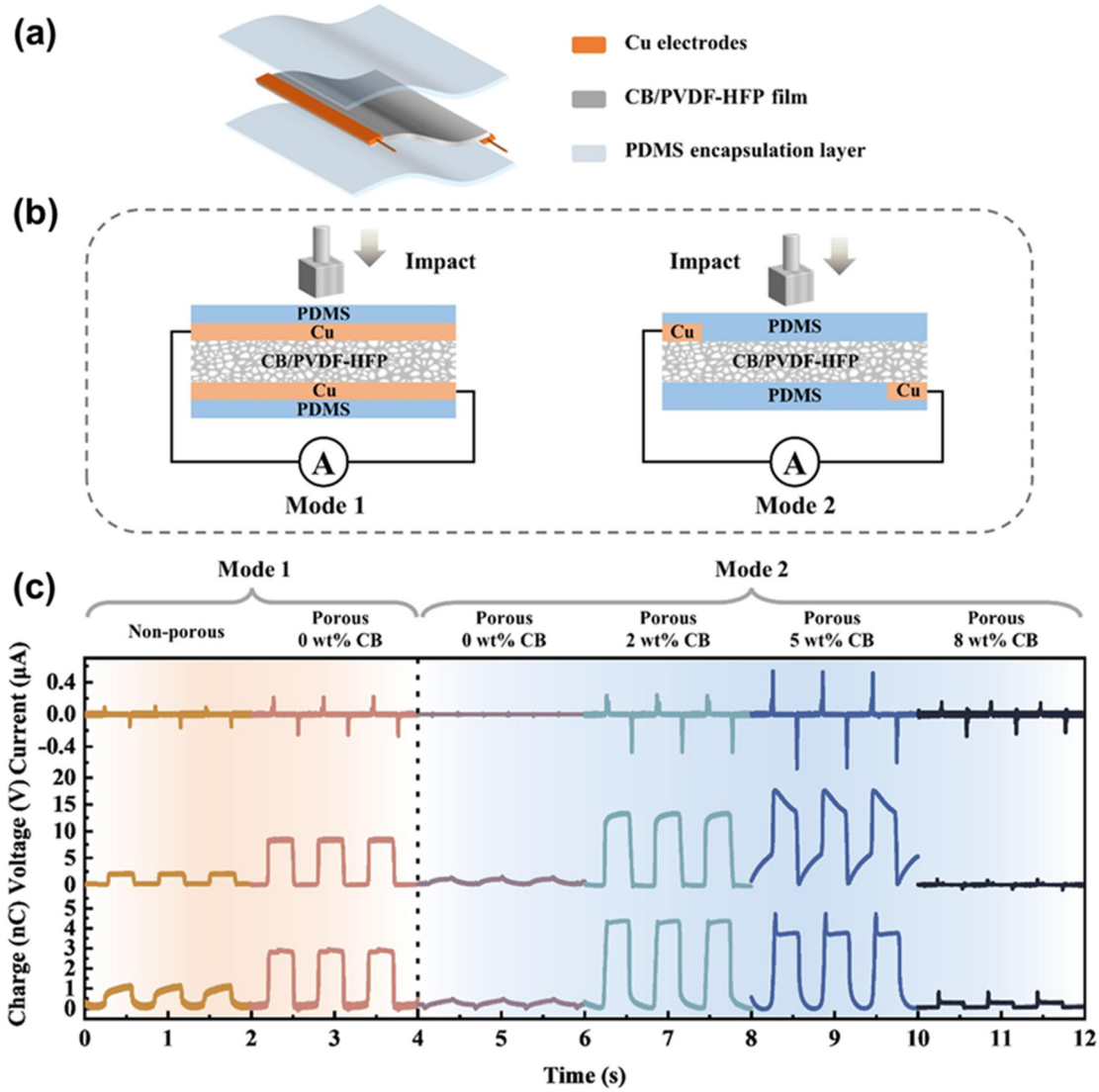

Fig. 5 (a) Schematic illustration of a self-powered flexible sensor. (b) Two testing modes of sensors with different electrode adhesion modes. (c) Piezoelectric currents, voltages, and charges generated by the non-porous pure PVDF–HFP film and porous CB/PVDF–HFP composite films. Reproduced with permission.[128] Copyright 2023 Elsevier B.V.

sided electrode-based piezoresistive sensor using CNT-incorporated polyurethane (PU@CNT) film. The synthesis process of the sensor is illustrated in Fig. 6a, and a digital photograph of the prepared sensor is displayed in Fig. 6b.[131] The different concentration of PU was taken in *N*,*N*-dimethylformamide (DMF) to generate a porous structure. Further, these films were dip coated in CNTs to fabricate different types of sensors. The relative change in resistivity was found to be increased for all the sensors under uniform pressure, as depicted in Fig. 6c.[131] The response of cyclic relative resistance changes with different applied pressure, as shown in Fig. 6d.[131] Film deformation takes place in the presence of external pressure, leading to an increase in the contact area between the electrodes and CNTs. This leads to an increase in the number of conductive pathways within the pores of the composite film, which results in a reduction of the resistance, as indicated in Fig. 6e.[131] In contrast with this, to investigate the effect of different concentrations of conducting materials in the polymer matrix, Jang and team developed piezoresistive sensors using CNT and carbonyl iron powder (CIP) incorporated in the polymer matrix. The schematic of the synthesis process and working mechanism of the sensor are represented in Fig. 6f.[132] The electrical conductivity of the polymeric composite increases with the concentration of CNT. The dramatic increase (more than 3 orders of magnitude) in conductivity was observed when CNT concentration increased from 0.5 wt% to 1 wt% while it increased by 0.5 order of magnitude when the concentration was increased from 1 wt% to 1.5 wt% (Fig. 6g). Therefore, the CNT content more than 1 wt% is favourable for the fabrication of the sensors. The electrical conductivity measurement of the prepared composites with increasing concentration of CIP and fixed content of CNT

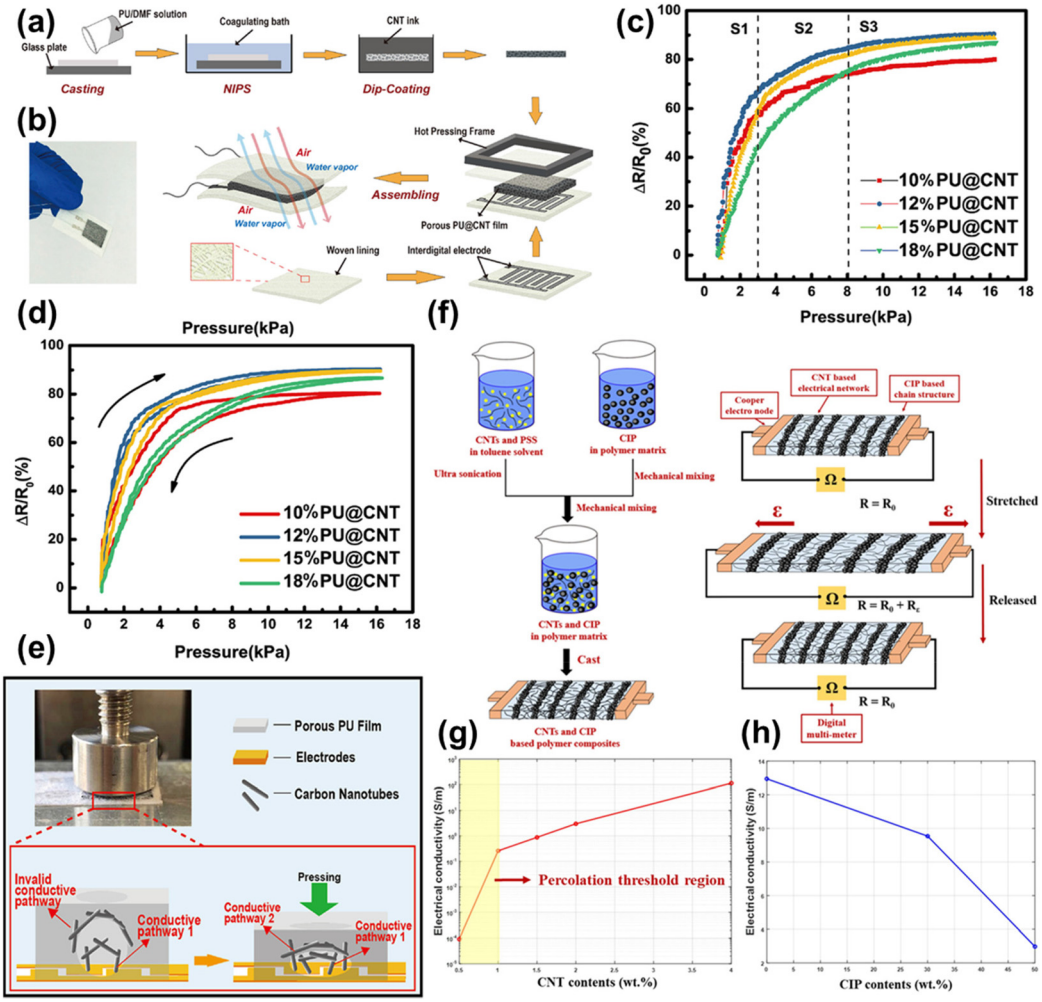

Fig. 6 (a) Schematic demonstration of the synthesis procedure of porous PU@CNT film and the piezoresistive sensor, (b) digital photographs of the prepared sensor. (c) The relative resistance changes with the increasing pressure of various PU@CNT sensors. (d) A cycle pressure–resistivity response of various PU@CNT sensors. (e) Schematic representation of the working mechanism of the PU@CNT sensor. Reproduced with permission from ref. 131. Copyright 2020 Elsevier Ltd. (f) Schematics of the manufacturing procedure and working principle of the polymeric composites. (g) The electrical conductivity of the polymeric composites with different CNT and (h) CIP contents. Reproduced with permission.[132] Copyright 2020 Elsevier Ltd.

(2 wt%) was also performed. The results indicated that the conductivity decreases with increasing concentration of CIP since the electric resistance of CIP is higher than that of CNT (Fig. 6h).[132]

In addition to CB and CNT, graphene, a 2D material consisting of sp^2-bonded carbon atoms is also a promising candidate for high performance sensors because of its high mechanical strength and electrical properties.[133,134] Additionally, it shows interfacial π–π interactions with styrene–butadiene–styrene (SBS) family or SBS-containing copolymers; therefore, it can be utilized as nanofiller/polymer composites for the fabrication of piezoresistive sensors.[135,136] However, the choice of nanofiller and its concentration is critical for desired application. In general, the graphene/polymer composite shows superior piezoresistive sensibility as compared to other nanocarbons.[137–139] A composite material, using tri-block-copolymer styrene–ethylene–butylene–styrene (SEBS) as a template and various graphene material like graphene nanoplatelets GO and rGO as nanofiller, had been prepared to develop piezoresistive sensors. The structure of various graphene-based materials and the schematic diagram of the synthesis procedure of the sensor is demonstrated in Fig. 7a and b, respectively.[140] An operational amplifier with voltage follower configuration was utilized as a sensing circuit in which the capacitor works as a low pass filter, as shown in Fig. 7c.[140] In order to investigate the suitability of the sensor, four sensors fabricated using rGO/SEBS composite had been placed at four fingers of a hand glove to record the movement of each finger, as displayed in Fig. 7d. The response of the sensors was measured in terms of resistance change, with the bending of all fingers at the same instant by closing the hand (Fig. 7e) and with the bending of the fingers one at a time (Fig. 7f).

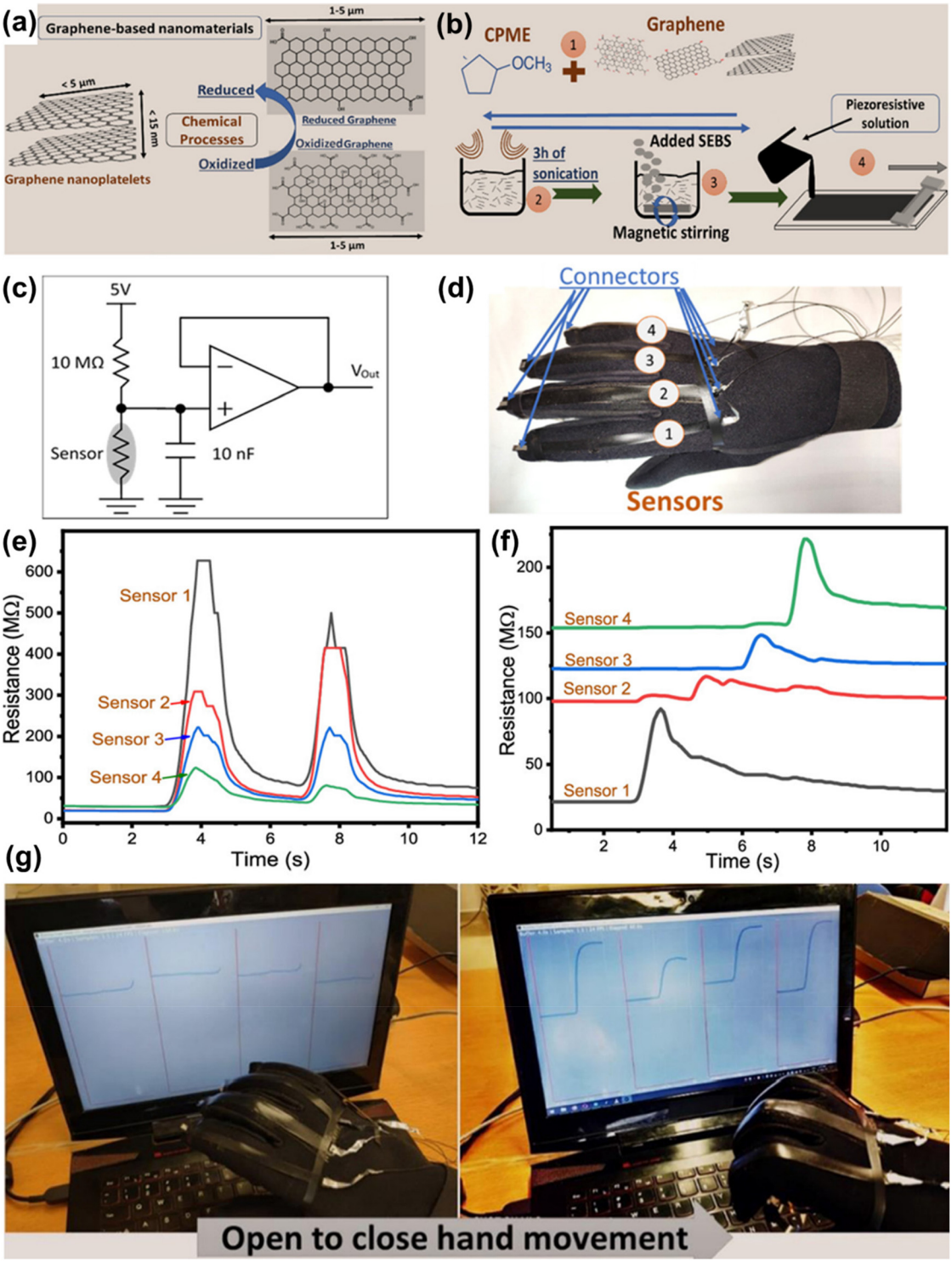

Fig. 7 (a) Illustration of the structure of the G-NPL, GO, and rGO nanomaterials. (b) Schematic representation of the processing method. (c) Signal conditioning circuit for each of the sensors. (d) Hand glove with four rGO/SEBS stripes placed over each finger. (e) Electronic readout of the resistance variation of the sensors when all fingers are moving at two different time points, and (f) for the sensors in each finger when moving separately. (g) Illustration of the hand glove application using four sensors, one for each finger. Reproduced with permission.[140] Copyright 2019 American Chemical Society.

Further, Fig. 7g indicated the rapid response of the sensor on the stretching of the rGO/SEBS composite film but due to the viscoelastic nature of the film, the recovery was slow.[140] Furthermore, Zheng *et al.* summarized the fabrication methods, selection strategies, and working principles of graphene-based sensors.[141]

CNTs exhibit excellent electromechanical properties, large aspect ratio, and high flexibility, which make it a potential material for flexible sensors. Furthermore, conducting CB particles are abundant materials having large surface area and low cost. By taking the mixer of both as nanofiller in the porous 3D structure, one can enhance the piezoresistive sensitivity. In this regard, CB particles and MWCNTs were mixed in the porous structure of polydimethylsiloxane (PDMS) to fabricate piezoresistive sensors, as depicted in Fig. 8a and b.[142] The schematic of the distribution of CB particles and MWCNTs and the working mechanism of prepared sensors, which is based on the tunnelling effect, is demonstrated in Fig. 8c.[142] The CB particle helps to increase the number of conducting paths on applying stress to the sensor. Fig. 8d represents the variation of current with applied voltage (*I–V* characteristics) of the sensor under various applied pressures. The curve shows ohmic characteristics under different pressures. Additionally, as the pressure increased at a fixed applied voltage, the current increased. This is because of the decrease in resistance due to the deformation of the CB/MWCNTs composite film.[142] The relative resistance *versus* pressure curve of various weight ratios of CB particles and MWCNTs (keeping total amount the same)-based composite is shown in Fig. 8e. An equal amount of CB particle and CNT-based pressure sensor showed the highest sensitivity. The elongation of CNTs with each other forms a conductive network due to its larger aspect ratio and higher conductivity than CB particles. The addition of CB particles in CNTs forms fragile CNTs–CB contact point, which helps to enhance the conductivity. When the amount of CNTs become higher, then more fragile CNTs–CB contact forms, but the reduction in contacts between CNTs resulting in a reduction in the conductivity.[142] The stress *versus* strain curve of the 1 : 1weight ratio of CNTs and CB (CB/MWCNTs = 1 : 1)-based sensor is plotted in Fig. 8f. The results showed that the composite film was torn when the strength reached 0.86 MPa, and the deformation reached 139%. Furthermore, the increase in relative resistance changes was observed with an increase in pressure (Fig. 8g), and the relative resistance change under

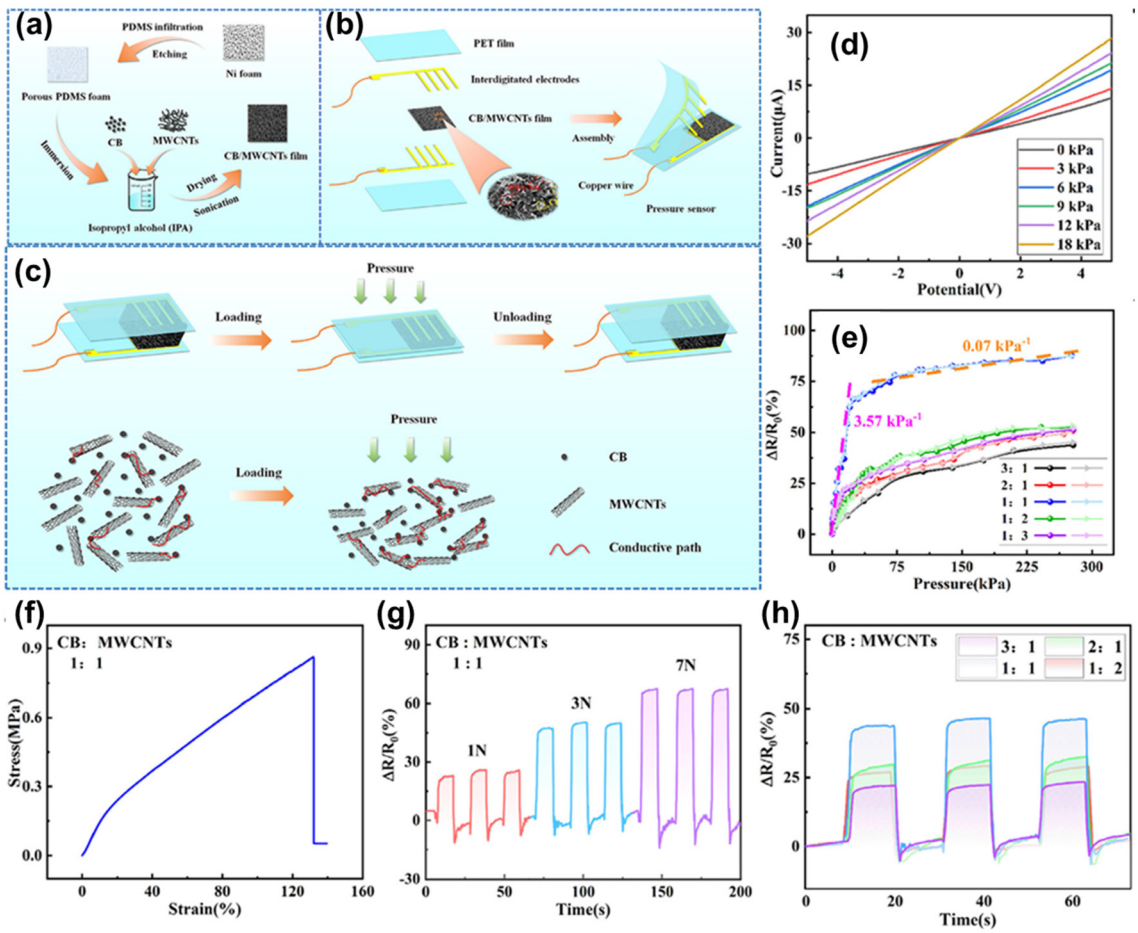

Fig. 8 (a) Fabrication procedure of the conductive film based on CB/MWCNTs. (b) Assembly of the pressure sensor based on CB/MWCNTs. (c) Schematic diagram of the working principle and hybrid conductive network constructed by the CB/MWCNTs composite. (d) Current–voltage (*I–V*) characteristic curves of the sensor under different applied pressures. (e) Sensor's relative resistance change ($\Delta R/R_0$) with different weight ratios of mixed conductive fillers in response to the applied pressure. (f) Stress–strain test curves of mixed conductive fillers. (g) Measurements of repeated loading/unloading experiments at different pressures. (h) Measurement results of repeated loading/unloading experiments at different weight ratios of CB and MWCNTs. Reproduced with permission.[142] Copyright 2022 The Authors. Published by American Chemical Society.

three N pressure of the sensor was manifest among different weight ratios of CNTs and CB composite-based sensors (Fig. 8(h)).[142]

The nanocomposite of zero-dimensional CB and two-dimensional nanomaterials graphene nanosheets (GNs) were also utilized to enhance the sensitivity of the piezoresistive sensor.[143–146] Additionally, the sensor based on the 3D structure offers more abundant sensing functions as compared to the sensor with lower dimensional structures but their complex synthesis route hinder their utilization. Ma *et al.* followed an effective 3D printing on SEBS substrate to fabricate CB/GNs composite-based piezoresistive sensors by three different routes, as demonstrated in Fig. 9a–d.[147] The relative change in resistance *versus* relative change in length and relative change in resistance *versus* pressure curves (Fig. 9e and f) were used to analyze the stretch sensing properties of the sensors.[147] The gauge factor values of the sensors CB/GNs@SEBS and GNs/CB@SEBS was found to be 10.89 and 2.81 under strain less than 50% while it was found to be 47.60 and 3.94 under strain are in the range of 50–100%, respect-

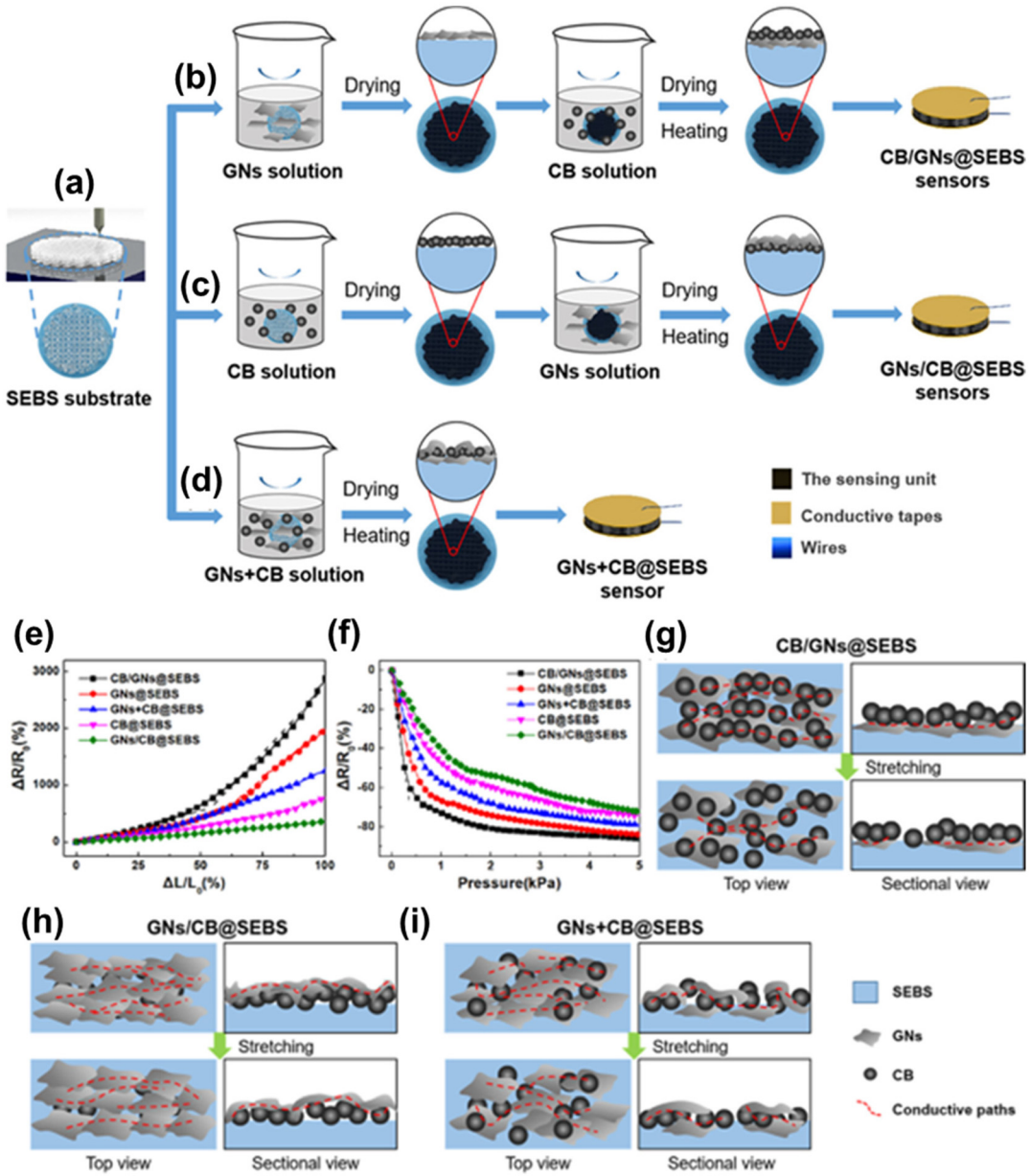

Fig. 9 Schematic illustration of the flexible piezoresistive sensor fabrication. (a) 3D printing of the SEBS substrate. Surface filling of the conductive nanomaterial composites of (b) CB/GNs@SEBS sensor. (c) GNs/CB@SEBS sensor and (d) GNs + CB@SEBS sensor. Resistance responses to various (e) $\Delta L/L_0$ under tension and (f) pressures under pressure. The top view (left) and sectional view (right) schematics of the conductive networks of (g) CB/GNs@SEBS, (h) GNs/CB@SEBS, and (i) the GNs + CB@SEBS in the initial state and the stretching state, respectively. Reproduced with permission.[147] Copyright 2022 American Chemical Society.

ively. The distribution and morphology of CB and GNs in the conductive network explains the stretch sensing properties of various sensors. In the CB/GNs@SEBS sensor (Fig. 9g), CBs are mainly distributed on the surface of GNs and have small impact on GNs morphology. Some CBs, which were dispersed between GNs, acted as connectors between adjacent GNs. This resulted in an easy disconnection of the conductive network, leading to a significant decrease in resistance during stretching. This sensor's sensing process was influenced by the quantum tunnelling effect. On the other hand, the GNs in the GNs/CB@SEBS sensor are noticeably wrinkled and curled because of the CB layer beneath them, resulting in a tight binding between conductive nanomaterials (Fig. 9h).[147] On stretching, the contact area between GNs was reduced as the GNs unfold, but it remains relatively large due to the properties of the 2D material. Consequently, the decrease in the number of conductive paths in the stretched state was not significant, which resulted in a linear decrease in resistance. The primary mechanism causing piezo-resistance in the GNs/CB@SEBS sensor was the reduction in the contact surface between conductive nanomaterials during stretching. In the GNs + CB@SEBS sensor, GNs and CBs have similar distribution as in both the CB/GNs@SEBS and GNs/CB@SEBS sensors (Fig. 9i). Therefore, the GNs + CB@SEBS sensor shows sensing ability in between the sensing ability of CB/GNs@SEBS and GNs/CB@SEBS sensor.[147]

3.2 Piezoelectric sensors

Nanocarbon-based piezoelectric sensors have advantageous unique properties of nanocarbons to enable the conversion of mechanical energy into electrical signals. These sensors offer enhanced sensitivity and responsiveness, making them compatible for detecting minute structural damage. Additionally, their robust mechanical properties ensure durability and reliability of the sensors in diverse environmental conditions.[110] The general principle of piezoelectric sensor is shown in Fig. 10a and b, which indicates that under mechanical stress, the deformation of non-centrosymmetric crystal structures causes the separation of electric dipole moments, resulting in the generation of a piezoelectric voltage on both sides.[148,152,154] Generally, the physical measurable quantity piezoelectric coefficient (d_{33}) determines the efficiency of energy conversion in the piezoelectric material. The introduction of nanocarbons in the composite structures provide more conductive pathways, which enhances the piezoelectric coefficient.[149] Li *et al.* reported the enhancement in piezoelectric properties of PVDF-*co*-trifluoroethylene (TrFE) on the incorporation of multi-dimensional nanocarbons.[150] The intrinsic graphene having center of symmetry does not show piezoelectric behaviour. However, the research reports that the modified or engineered structure of graphene exhibits piezoelectric responses.[151] Furthermore, incorporation of these materials in the piezoelectric composite improves the response of pressure sensors. For example, rGO-wrapped PVDF nanofiber films were deposited on a PDMS substrate to develop a pressure sensor, as demonstrated in Fig. 10c. The number of conducting pathways in the sensor increases; therefore, more current is generated under loading. Upon unloading, the PDMS returns to its initial state, resulting in a decrease in current (Fig. 10b). The *I–V* characteristics of the PVDF@rGO composite under various pressure situations shows stable ohmic behaviour, as illustrated in Fig. 10d. Under high pressure, the relative change in current increases rapidly with a change in pressure (Fig. 10e). However, the sensor shows excellent linear response under low-pressure regime (inset of Fig. 10e). The current increased on loading of 8 mg feather and further increased on loading 20 mg rice on the sensor, which indicated that the sensor might be used to detect a minute change in pressure with fast response (Fig. 10f).[152] The conventional pressure sensors pose difficulties to respond to static signals that rely on the transient flow of electrons under external pressure due to the piezopotential produced by dynamic stress. Graphene-based sensors are able to measure static pressure with high sensitivity and fast response. Fig. 10g represents the linear response of change in current as a function of applied pressure for Pt nanowire/graphene sensor. Furthermore, the sensor shows reversible behaviour under stretching and release conditions, and the low hysteresis observed can be ascribed to the elastic deformation and viscoelastic effects inherent in the device. The low hysteresis indicated the fast response of the device. The loading and unloading cycle response for static pressure is depicted in Fig. 10h, which indicating a decrease in current response under applied force and retains its initial value when force was removed.[153]

Graphene plays a significant role in designing wearable stretchable piezoelectric sensors. Huang *et al.* designed a sensor with high sensitivity and low detecting threshold by coating PVDF/graphene composite on commercially-available polyester fabric.[155] The prepared sensor generates high voltage as compared to the PVDF film and PVDF-coated polyester fabric (Fig. 10i). The fabric provides intense voltage, whereas the introduction of graphene enhances the piezoelectric performance. Fig. 10j demonstrated the response of the sensor on hitting the front and backside of the sensor, indicating the reversibility of indirect dipole moment in PVDF. Additionally, the sensor shows linear response under external applied force in the range of 0.05–0.45 N (Fig. 10k) as well as excellent satiability up to 125 cycles under successive electromagnetic punch (Fig. 10l).[155]

3.3 Capacitive sensors

In the realm of SHM, the integration of nanocarbon-based capacitive sensors also represents a groundbreaking approach. Capacitive sensors exhibit a parallel plate arrangement, where the dielectric surface is sandwiched between the coupled electrodes (Fig. 11a).[154,156] The electrical properties of nanocarbons are altered under mechanical stress, which results in capacitance variations. These changes are then translated into actionable data for structural health assessment. The capacitive sensor utilizing a singular suspended graphene membrane is relatively diminutive compared to commercially-available sensors. However, double layer graphene (DLG) membrane

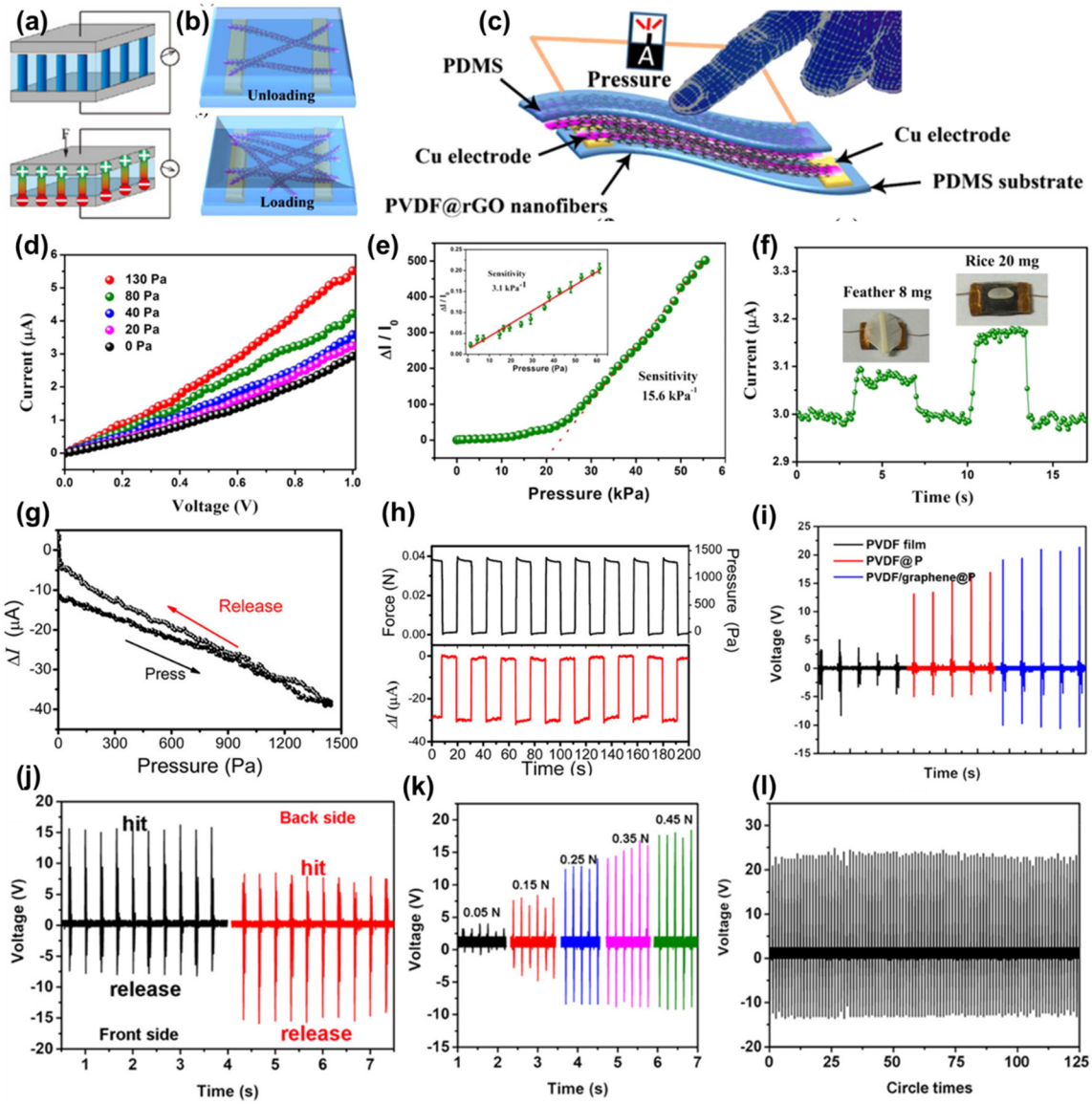

Fig. 10 (a) Schematic illustration of the piezoelectric mechanism. Reproduced with permission.[154] Copyright 2017 Elsevier Ltd. (b) Graphical representation of the conducting pathways under loading and unloading. (c) Schematic of the graphene-based pressure sensor. (d) *I*–*V* curves of the device under different pressure loading conditions. (e) Current response ($\Delta I/I_0$) *vs.* applied pressure. The inset shows the current response curve below 60 Pa. (f) Transient response to the loading and removal of a feather (8 mg) and a rice (20 mg), the fronted corresponding to a pressure of only 1.2 Pa. Reproduced with permission.[152] Copyright 2016 Elsevier Ltd. (g) Current change of the PTNWs/G pressure sensor during the press and release process and (h) current response under the pressure cycles. Reproduced with permission.[153] Copyright 2017 American Chemical Society. (i) Voltage output of PVDF film, PVDF@P, and PVDF/graphene@P. (j) The voltage signals of hitting the front (black signals) and back (red signals) side of PVDF/graphene@P. (k) The relationship between voltage output and different strength input (from 0.05 to 0.45 N), and (l) more than 125 cycles of voltage output illustrating the durability of PVDF/graphene@P. Reproduced with permission.[155] Copyright 2018 American Chemical Society.

supported on a PMMA layer-based capacitive sensor showed superior sensing ability even after a high annealing temperature. To improve the performance of sensors, the thickness of the transferred polymer layer was reduced by annealing, as demonstrated in Fig. 11b. The linear response of the sensor was observed for $|\Delta P| < 200$ mbar. In Fig. 11(c), the dashed magenta line represents maximum theoretical response of a sensor at a perfect yield of intact hermetic drums of 100%, whereas the solid magenta line is the theoretical fitted curve with the observed data at a yield of 25%.[158]

CNT is also utilized as a capacitive sensor for SHM. A schematic of CNT–PVDF composite nanofiber membrane-based capacitive sensor is demonstrated in Fig. 11d. The interfacial polarization in the composite nanofiber in the presence of electric field plays an important role to improve the permittivity. The distance between electrodes decreased from d to d′

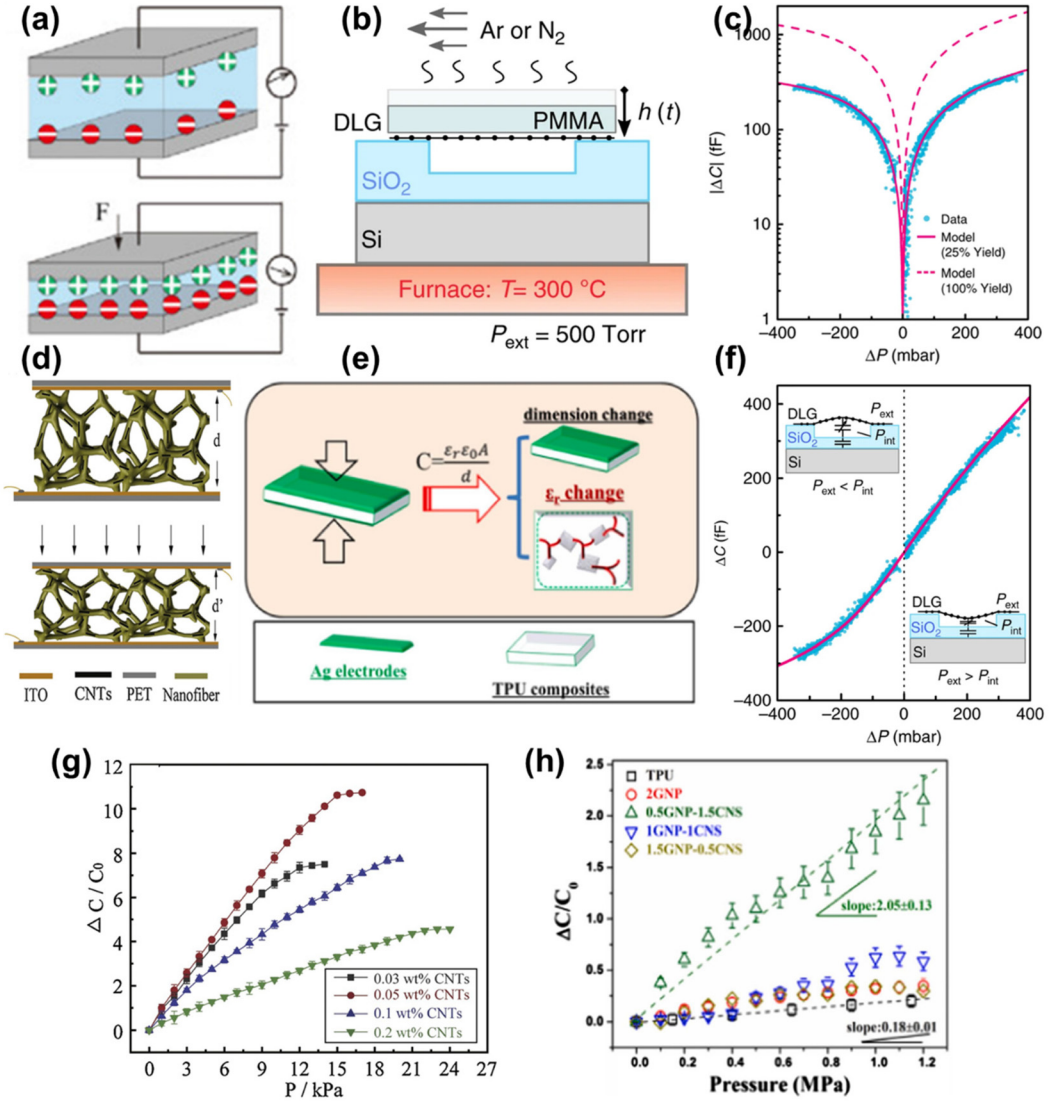

Fig. 11 (a) Schematic illustration of the piezocapacitive mechanism. Reproduced with permission.[154] (b) Schematic explanation of the thermal annealing principle applied to reduce the PMMA thickness. (c) Comparison, on a log-scale, of the measured data (blue points) to the model with 100% (magenta dashed line) and 25% (solid magenta line) yield of the hermetic drums using the 2D Young's modulus. (d) Sensing mechanism of CNT–PVDF capacitive pressure sensor.[158] (e) Mechanism illustration of the capacitance change in TPU composites responding to pressure.[160] (f) Capacitance–pressure curve for the DLG sensor. Reproduced with permission.[157] (g) The relative change in capacitance of the sensor with different weight ratio CNTs addition under pressure applied. Reproduced with permission.[158] Copyright 2019 Elsevier B.V. (h) $\Delta C/C_0$ plotted with pressure for TPU and its composites. Reproduced with permission.[160] Copyright 2019 Published by Elsevier Ltd.

under external pressure (Fig. 11d); as a result potential difference increased and thus polarization also increased.[158] The proposed mechanism of the sensor is illustrated in Fig. 11e.[160] The change in capacitance with respect to change in pressure is depicted in Fig. 11f.[157] The electric field becomes sharper due to enhanced polarization, which further increases permittivity. In addition, the dense distribution of CNT in the CNT–PVDF composite may also increase the permittivity of the composite. The change in capacitance with applied pressure for varied concentrations of CNTs in PVDF is plotted in Fig. 11g. The results showed that as the pressure increased, the separation between electrodes decreased; therefore, the capacitance increased immediately. Furthermore, the sensitivity was found to be maximum for the sensor prepared with 0.05 wt% CNT addition of PVDF.[158] Instead of the polymer, the composite of CNT and silicon rubber was utilized as a dielectric layer to develop a stretchable pressure sensor. The prepared sensor showed excellent stable sensing and repeatability with minor hysteresis effect.[159] Another high-performance pressure sensor was developed by mixing different compositions of CNT and graphene nanoplatelets in thermoplastic polyurethane (TPU) for tuning the dielectric properties. The variation of relative change in capacitance with pressure for the prepared sensors is depicted in Fig. 11h, indicating that the sensor prepared

with the 0.5GNP–1.5CNS composite showed the highest change in relative capacitance. During compression, the sensor's thickness diminishes and the surface area undergoes a slight increase, which leads to an increase in the polarization and hence an increase in capacitance.[160]

3.4 Triboelectric sensors

Generally, electrical charges are induced on the surfaces of two different materials when they rub with each other. The amount of induced charge significantly depends on the triboelectric polarities difference between the contacting materials.[161] The triboelectric sensors transform mechanical energy into electrical energy. The general working mechanism of these sensors is demonstrated in Fig. 12a.[154] Initially, two materials with different triboelectric polarities have small gaps. Under external pressure, the materials come in contact with each other, and opposite charges are induced on their surface due to the triboelectric effect.[162] On releasing the pressure, the surfaces carrying opposite charges autonomously separate, generating compensating charges on each side of the top. Due to the existence of an air layer between the materials, the complete neutralization of charges on the two surfaces is not achieved, which leads to the formation of a potential difference. Based on this mechanism, a multiple layer of rGO

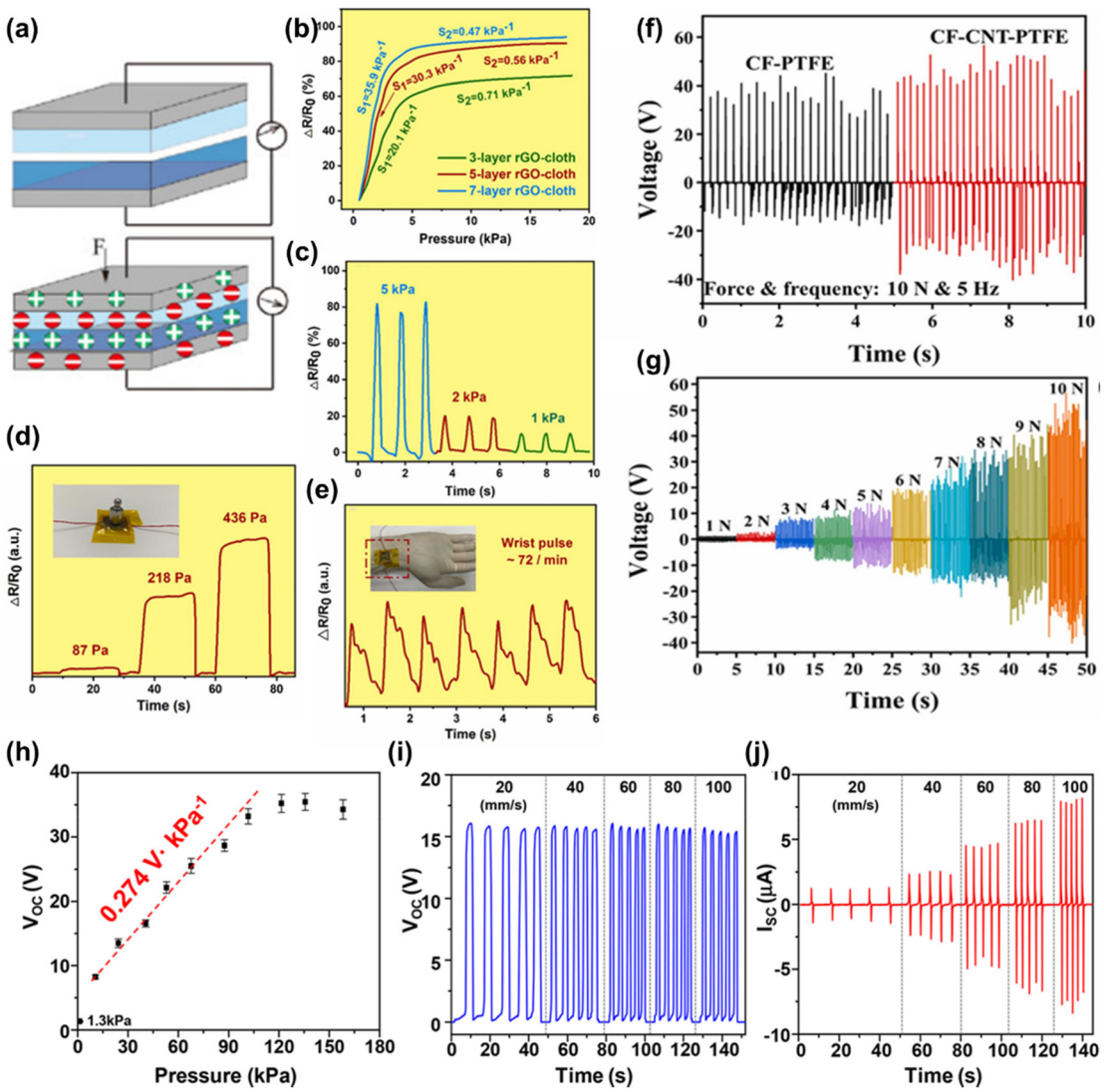

Fig. 12 (a) Schematic illustration of the triboelectric mechanism. Reproduced with permission.[154] Copyright 2017 Elsevier Ltd. (b) Rate of resistance change with pressure increases for the 3-layer, 5-layer, and 8-layer rGO-cloth/LIG pressure sensors. (c) Response test of the 5-layer rGO-cloth/LIG pressure sensor to different pressures. (d) Response of the rGO-cloth/LIG pressure sensor under different pressures. (e) Response of the rGO-cloth/LIG pressure sensor for wrist pulse.[163] Copyright 2022 Published by Elsevier Ltd. (f and g) Triboelectric performances of the fabricated CF-CNT TENG device. Reproduced with permission.[164] Copyright 2023 Elsevier Ltd. (h) The V_{OC} according to pressure. (i and j) V_{OC} and I_{SC} current depending on touch velocity from 20 to 100 mm s^{-1}. V_{OC} remains constant within the standard deviation of 0.13 with touch velocity, and ISC increases with touch velocity. Reproduced with permission.[165] Copyright 2019 Elsevier Ltd.

cloth-based triboelectric pressure sensor was designed by laser-induced graphene. The seven layers of rGO cloth-based sensor showed highest sensitivity in the small pressure range, as shown in Fig. 12b. The sensitivity of the sensor increases with increasing number of layers and gradually becomes saturated. Fig. 12c further confirms that the relative resistance change was stable for different pressures under repetitive loading–unloading. In addition, Fig. 12d shows rapid and stable response under varying pressures. The outcome of the wrist pulse test is depicted in Fig. 12e, which demonstrates that the pressure sensor exhibits a commendable response to the wrist pulse. Furthermore, the test curve implies a pulse rate of approximately 72 beats per minute, which is consistent with the typical range for a healthy human body.[163]

The introduction of CNT in two different materials enhances the triboelectric properties. The cigarette filters (CF) are generally discarded as the waste is utilized to develop a triboelectric nanogenerator (TENG) device. The electric performance of the device was examined after adding 0.1 wt% CNT, as shown in Fig. 12f. The results indicate that CF-CNT-based TENG device showed excellent triboelectric performance than CF-based TENG. Fig. 12g demonstrated that the output voltage of the CF-CNT-based TENG device increases with increasing pressure.[164] Graphene can also be utilized as an electrode material to fabricate self-powered triboelectric pressure sensors. A single electrode structure of a pressure sensor was designed by using the deposition of atomically-thin graphene electrode on the electrification layer of PDMS, where polyethylene terephthalate was used as a substrate. The change in output voltage (V_{OC}) as a function of touch pressure is plotted in Fig. 12h. The variation in V_{OC} with touch pressure occurs not only due to a variation in the surface area but also the deformation of PDMS. The sensors provide stable response under varying tapping speed (Fig. 12i), and the current (I_{SC}) through the sensor increases with an increase in tapping speed (Fig. 12j).[165] Furthermore, graphene oxide/porous PDMS can be utilized as a compound friction layer in the fabric-based triboelectric nanogenerator.[166] The above discussion indicates that nanocarbon materials are permissible for the fabrication of a triboelectric pressure sensor for SHM.

3.5 Raman analysis

Smart biocomposite materials with inbuilt SHM sensors are able to control stress-transfer between the fiber and the matrix. Understanding the interfacial failure and damage detection at an earlier stage and real time is of paramount importance for their real-world applications. Raman spectroscopy is one of the most employed techniques to analyze local strains in composite materials due to a non-destructive and non-invasive technique. However, this technique is restricted only up to Raman-sensitive materials. This issue can be overcome by the introduction of Raman-sensitive fibers as a SHM sensor in the vicinity of Raman-insensitive reinforcing fibers or matrix. The sensing of strain/pressure using Raman spectroscopy is a wireless technique unlike electrical methods. In a Raman strain sensor, the change in vibrational frequency is measured when the material is subjected to mechanical strain. Under strain, the molecular and crystal lattice structure of the material can change, which can lead to a shift in vibrational frequencies. The amount of strain or stress can be determined by analyzing these frequency shifts. The nanocarbon-based strain sensor showed a linear shift in their G band of Raman spectra under external strain.[167–170]

Tsirka *et al.* fabricated a multifunctional structure onto CF by growing MWCNT using chemical vapour deposition (CVD) at different temperatures and time for strain sensing applications. The prepared samples were named as CF-CNT@temperature/time, where temperatures were in degree centigrade and time in minutes. The Raman shift *versus* applied strain calibration curve for CF, CF-CNT@750/30, and CF-CNT@850/30 is shown in Fig. 13a. The Raman sensitivity of each morphology was evaluated by linear fitting of the experimental observed data. A 34.3% and 87.4% increment in Raman sensitivity was observed for CF-CNT@750/30 and CF-CNT@850/30 morphology, respectively, as compared to CF, attributed to a higher graphitization at higher temperature.[171] As compared to CNTs, 2D graphene is more preferred for Raman-active sensing applications because of the presence of high intensity of the Raman 2D band, which is quite sensitive to strain or other variations.[172,173] Taking this advantage, three different types of graphene materials such as Elicarb graphene, exfoliated graphene (EG), and CVD-grown graphene were utilized to develop glass fiber/epoxy model-based Raman-strain sensors. The schematic of prepared sensors is depicted in Fig. 13b.[174] The inset in Fig. 13c and d represent the surface morphology (SEM image) of Elicarb graphene and EG-coated glass fiber, respectively. To analyze the sensing performance of Elicarb and exfoliated graphene-coated glass fiber, Raman 2D band positions were recorded under different tensile strain (Fig. 13c and d).[174] A linear shift in the Raman 2D band toward lower wavenumber indicates the transfer of stress from the fiber to the coating layer. Additionally, EG-coated glass fiber showed higher strain rate shift as compared to Elicarb graphene-coated glass fiber. Enhanced interaction between the flakes, fibers, and epoxy coating and higher aspect ratio were attributed to enhanced stress transfer in EG-coated glass fiber. This results from the functionalities on the graphene plane, which have the potential to react with the epoxy resin and the surfaces of the fibers. Moreover, a significant enhancement in the shift rate was also observed under strain after the embedment of EG-coated glass fibers into the epoxy resin matrix (Fig. 13e). This setup simulated a model composite consisting of a single fiber filament since the Elicarb graphene and EG have limited aspect ratio and inconsistent properties, which may hinder their sensing ability.[174]

A strain sensor composed of graphene coated on glass fiber using CVD was also designed. The shift in Raman 2D band under 0.2% strain was observed for the CVD graphene-coated glass fiber after embedding into the epoxy matrix (Fig. 13f and g). The surface morphology of CVD graphene-coated glass fiber is shown in the inset of Fig. 13g. Furthermore, the cycle study for five loading/unloading cycles under 0.4% strain

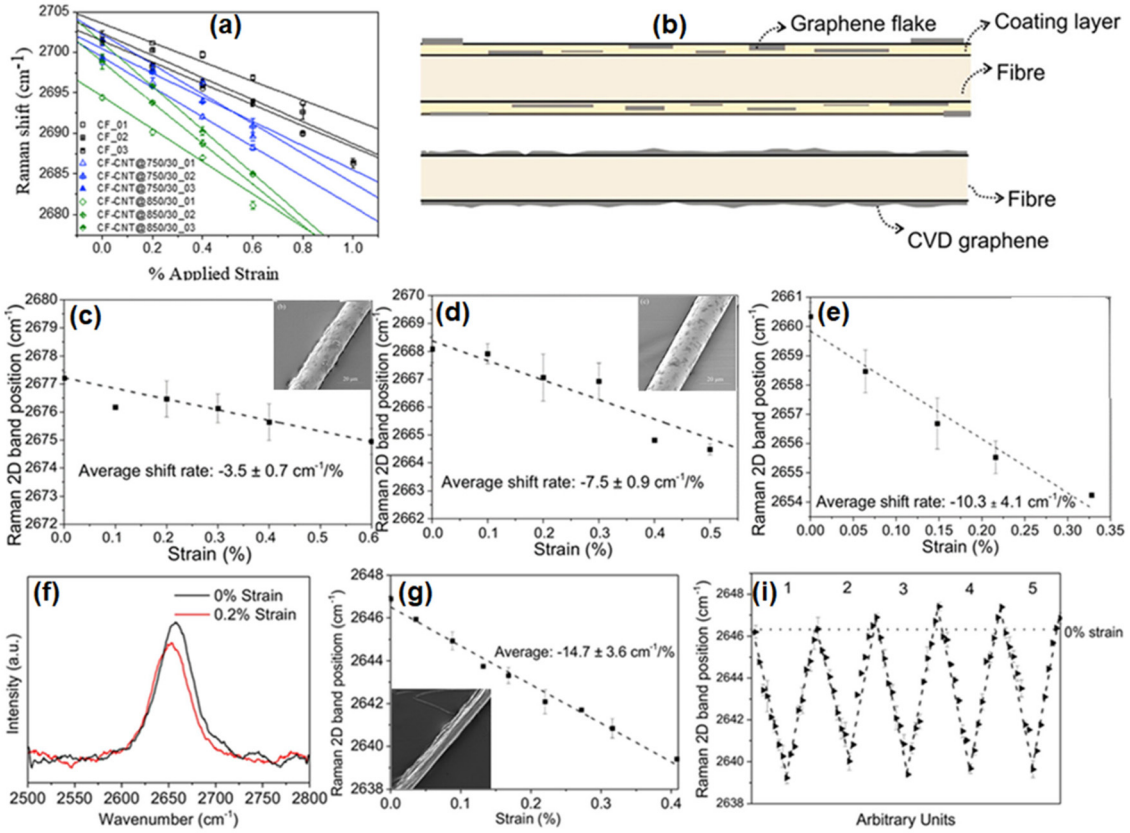

Fig. 13 (a) Raman shift *vs.* strain calibration curves. Reproduced with permission.[171] Copyright 2018 Elsevier Ltd. (b) Schematic illustration of glass fibers coated with graphene flakes (top) and CVD graphene (bottom). Raman 2D band position of (c) Elicarb and (d) EG graphene coated onto glass fiber surfaces with respect to applied strain before being embedded in the epoxy resin matrix (insets are respective SEM images). (e) Raman 2D position shift with strain for EG-coated glass fiber after embedment. (f) Raman 2D peak position before and after deformation. (g) 2D band shift with respect to strain (inset is the SEM image of the CVD graphene-coated glass fiber), and (i) five cyclic deformations to about 0.4% strain and the response of 2D band position for the CVD graphene-coated glass fiber. Reproduced with permission. Reproduced with permission.[174] Copyright 2019 American Chemical Society.

(Fig. 13i) shows the elastic deformation of CVD graphene-coated glass fiber without any damage.[174]

3.6 Field-effect transistor

A field-effect transistor (FET) is a single-junction three terminal (source, drain, and gate) electronic device, which is used in the amplification and switching of electronic signals. Recently, FET as a pressure sensor has become a research hotspot in the field of SHM of smart biocomposite because of its high signal-to-noise ratio and easy integration on a large scale. The architecture of the FET sensor can be adjusted by the channel material and the structure of the device depending on the sensing of the type of stimuli. Fig. 14a represents the schematic of the general mechanism of the FET sensor, current–voltage (*I–V*) characteristics, and various FET-based sensors. The drain current (I_D) is controlled by the electric field at the gate terminal. Furthermore, the electrical properties of the sensor depend on the type of electrode material, type of semiconductor material in the channel region, and capacitance of dielectric material. Under external pressure, the properties of components used in device are changed, which results in a change in the *I–V* characteristic of the device.[175] CNTs exhibited high charge carrier mobility and excellent mechanical flexibility, which make them potential material for a high performance FET strain sensor.[176,177] Cheng *et al.* fabricated an FET pressure sensor on a SiO_2/Si substrate using CNTs as a channel material and a 3D pressure sensitive top gate electrode, as displayed in Fig. 14b. The surface morphologies of the top-grid electrode CNTs are depicted in the SEM images (Fig. 14c). The pressure sensing mechanism of the prepared sensor is based on the capacitance, as illustrated in Fig. 14d. In the absence of external pressure, there is almost no contact between the top electrode and the sensor. Consequently, the predominant factor affecting the capacitance was the presence of an air gap. However, when pressure was applied, the contact area between the dielectric layer and the pyramid-shaped top electrode structure expanded, which led to a notable elevation in the micro-structured elastomer capacitance. Therefore, the changes in applied pressure on the top electrode resulted in the corresponding changes in the drain current.[178] Fig. 14e represents the total simulated capacitance between top electrode and trench when the sensor was

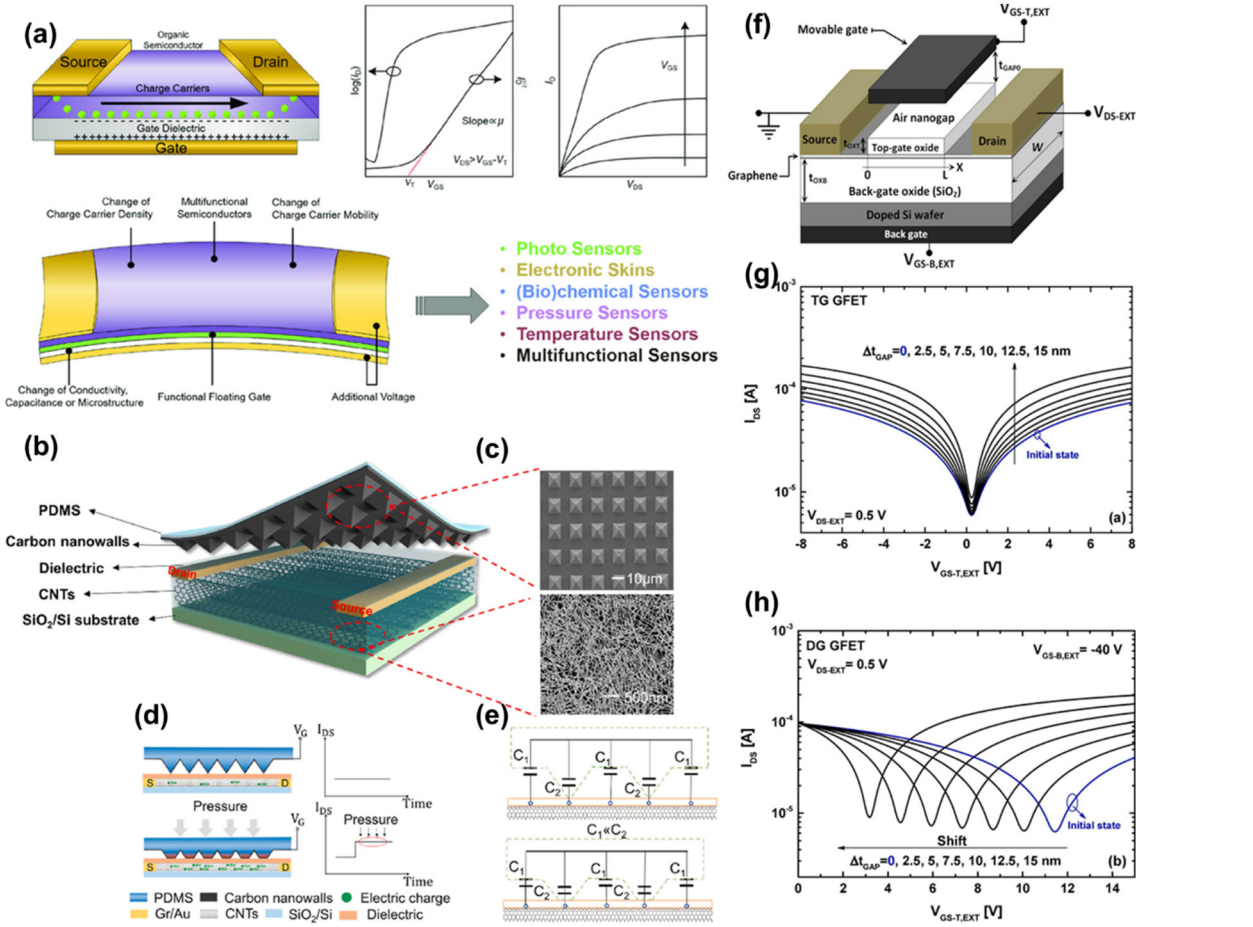

Fig. 14 (a) Mechanism of typical FET, *I*–*V* characteristics, and FET-based sensors. Reproduced with permission.[175] Copyright 2020 The Authors. Published by Wiley-VCH Verlag GmbH & Co. KGaA, Weinheim. (b) Schematic diagram of CNTs–FET sensor based on 3D conformal force-sensitive gate electrode. (c) SEM images of the pyramidal microstructure 3D conformal force-sensitive gate electrode (scale *d* = 10 μm) and the CNTs film (scale *d* = 500 nm). (d) Schematic diagram of the initial state of the sensor and the loading pressure state and (e) circuit structure diagram of the sensor. Reproduced with permission.[178] Copyright 2023 Elsevier Ltd. (f) Three-dimensional (3D) structure of the proposed dual-gate GFET-based pressure microsensor. Transfer characteristics of the proposed pressure sensor as a function of pressure-induced gate displacement considering (g) top gate GFET and (h) dual gate GFET. Reproduced with permission. Reproduced with permission.[183] Copyright 2020 Elsevier GmbH.

in the initial state and under pressure, where C_1 represents the micro-structured elastomer capacitor and C_2 is air-gap capacitor.[178]

Apart from CNTs, graphene also has high mobility, high mechanical strength, high carrier mobility, and low cost, which makes it suitable for employing as a channel of FET.[179–182] Yogeswaran *et al.* developed a biodegradable piezoelectric material-based extended gate FET pressure sensor. The low operating voltage make this device energy efficient, and the biodegradability of the material is useful for the reduction of electronic waste.[180] Furthermore, a dual gate-based graphene-FET (GFET) pressure microsensor model was proposed in which the sensing principle employed for the detection of nanoscale displacements induced by pressure relies on the utilization of a movable top gate concept (Fig. 14f). The operational principle of dual gate GFET is based on top capacitance modulation. The total capacitance of the top is series equivalent to top-oxide and nanogap capacitance. The top capacitance modulation caused by the external pressure applied to the movable gate's top surface results in a modification of the top electrostatic gating, subsequently leading to a variation in the drain current of the GFET. Fig. 14g represents I_D *versus* V_{GS} (gate to source voltage) curve as a function pressure-induced Δt_{GAP} (gap thickness difference before and after applied pressure) for the top gate FET model. The results show that the drain current increases with applied pressure at all values of V_{GS}. Further, no obvious change in the position of Dirac point (minimum drain current point) confirms the transition of the charge carrier through electrostatic gating. Similarly, the transfer characteristics (I_D *versus* V_{GS} curve) at different Δt_{GAP} for dual gate GFET model is shown in Fig. 14h.[183] In this case, a shift in Dirac point in the negative direction is observed on increasing the pressure or Δt_{GAP}. This characteristic was attributed because of the overlap of the electrostatic potentials generated by both the top and back gates within the graphene structure. Note that the pressure-

induced decrease in gap thickness made the top-gate electrostatic control more impactful on the channel while also modulating the effect induced by the back-gate voltage on channel; thus, the change in drain current becomes significant and a shift in Dirac point is recorded accordingly. Therefore, by monitoring the change in the position of Dirac point voltage and/or change in I_D, the applied pressure on the top movable gate can be sensed successfully. Therefore, dual-gate GFET model shows better sensitivity as compared the top-gated GFET model.[183]

4. Nanocarbon-based electronic skin

Electronic skin (e-skin), also known as e-skin or electronic dermis, is a thin and flexible electronic material that can have sensing capabilities as human skin. E-skin technology holds great promises in various applications including healthcare, robotics, and human–machine interfaces because it can detect and respond to various stimuli, such as pressure, temperature, humidity, and even chemical changes. E-skin can be made from biocompatible flexible material, which allows comfort with irregular shape and movement with the body. In addition, e-skin consists of sensors that can detect various physical and chemical stimuli. The majority of these reported flexible sensors are designed to detect the sole stimulus, which makes it challenging to meet the human demand for simultaneously sensing multiple stimuli. Therefore, over the recent years, an effort has been made for the development of versatile flexible sensors capable of detecting multiple external stimuli simultaneously. Furthermore, the ultimate goal for an ideal flexible sensor is to function effectively under extreme deformation conditions, severely worn, low power supply, or when implanted inside the body. This requires durability, portability, biocompatibility, and environmental friendliness of the sensors. To tackle these challenges, different materials have been employed in the design of multifunctional sensors such as nanocarbons,[184,185] ionic liquid,[186,187] conductive polymers,[188,189] and metal nanomaterials.[188,190] Among them, nanocarbons are quite attractive because of their low-toxicity, superior electrical conductivity, high thermal stability, and flexibility.[191] Carbon-based materials have been utilized in multifunctional sensors with different sensing models such as dual model, triple model, and multi model sensor.

The primary function of human skin is tactile perception, which refers to ambient pressure and perception of its own deformation. Therefore, dual model pressure–strain sensors with excellent performance are required to develop an efficient interaction with surroundings like human skin. Among different nanocarbons, SWCNTs are assumed as ideal materials for e-skin applications because of their superior properties such as high conductivity, mechanical strength, high flexibility, and piezo-resistivity.[192] Dual model pressure–strain sensors have been developed by combining CNTs-composite in a micro pillar-based hybrid structure. The fabricated sensors showed excellent sensitivity in a broad sensing range with a gauge factor of 707 for these two stimuli. Motivated by hairy skin, Zhang and team prepared similar dual mode sensor using two layers of CNTs/GO hybrid 3D conductive networks, which was assembled on a thin, permeable polydimethylsiloxane (PDMS) layer through a porogen-assisted self-assembly technique, as depicted in Fig. 15a. The prepared sensor produces response to wrist pulse, human breathing, and music rhythm in the noncontact mode by opposite resistance change under normal and tangential forces, respectively.[193] A dual-functionality sandwich structure of a GO-based humidity sensor and SWCNT-based pressure sensor utilizing screen-printing and inkjet printing processes was fabricated. Notably, SWCNTs served as the electrodes for both of these sensors, as depicted in Fig. 15b. The designed sensor showed excellent sensing ability toward different human activities such as breathing, palm sweat, and pulse.[194]

Temperature holds a significant connection with human life as it is a crucial parameter for assessing human well-being and monitoring the environment in our surroundings. Beyond the sensing of pressure and strain, temperature detection is also an essential function of human skin. It offers diagnostic information about an individual's health and acts as a safeguard against extreme temperatures. Harnessing the benefits of thermo-resistivity and piezo-resistivity of reduced graphene oxide dual model pressure/strain-temperature sensors were developed on a rGO-paper composite.[195,196] The device exhibited gauge factors of 7.99 and 18.96 under tensile and compressive strains, respectively. In addition, its resistance decreased by 11.3% when the temperature changed from 27 to 65 °C. Notably, the sensor had the capability to convert absorbed photon energy into thermal energy, which leads to a deformation in its shape. Furthermore, Li *et al.* fabricated multiwalled CNTs/PDMS fibers using the one-step extrusion method.[229] The resistance changes of the prepared sensor showed linear dependence on temperature in the range of 0–100 °C and strain from zero to 120%. Aside from the resistive type, capacitive sensors have also garnered significant attention in research because of their simple structure, swift dynamic response, and minimal power consumption. As demonstrated in Fig. 15c, microfluidic technology-based vertical/lateral pressure–temperature capacitive sensor was developed by CNTs/PDMS composites (CPCs). In the device, CPCs served as dielectric layer whereas ionic liquid acted as the electrode of the microfluidic channel.[197] As external pressure was applied, it changed the spacing between the micro-capacitors within CPCs, which led to fluctuations in both dielectric properties and conductivity. Moreover, as the temperature changes, there is a possibility of freely moving ions accumulating on the surface of the CPCs, consequently increasing the interface capacitance. When the device was affixed to both a bottle and human skin, it effectively monitored these two stimuli. Utilizing a solitary electrical signal change to simultaneously convey both pressure and temperature inherently leads to signal crosstalk, making it difficult to precisely discern the nature and magnitude of each stimulus in real time. To attain the segregation of output signals, a dual model

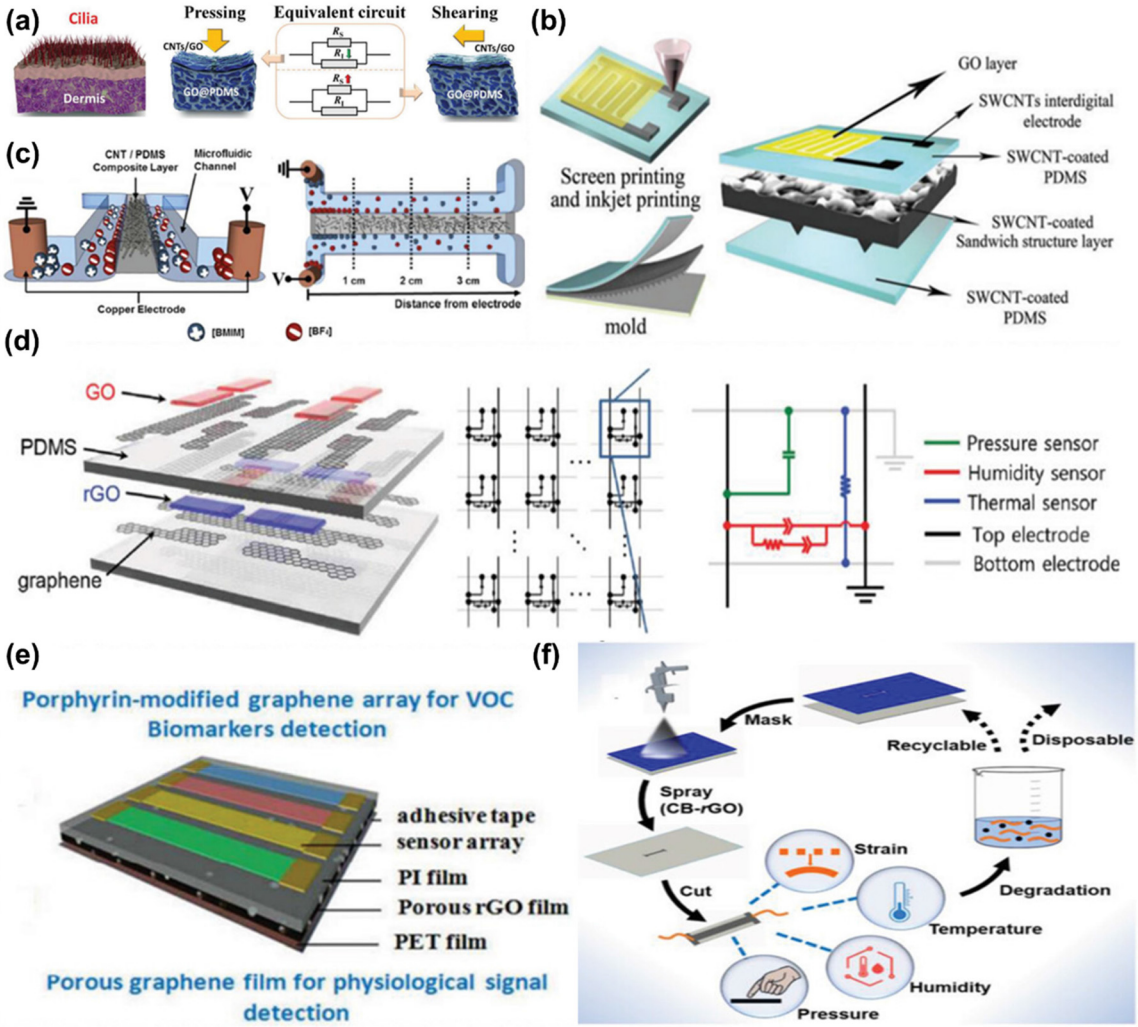

Fig. 15 (a) The CNTs/GO@PDMS-based sensor is analogous with the structure of hairy skin, and the corresponding resistance change in the equivalent circuits of the sensor under normal press and lateral shear force, Reproduced with permission. Reproduced with permission.[193] Copyright 2018 Wiley-VCH Verlag GmbH & Co. KGaA, Weinheim. (b) Diagram of the humidity sensing section (upper left) and pressure sensing section (bottom left) of the dual-modal sensor, reproduced with permission. Reproduced with permission.[194] Copyright 2020 Wiley-VCH Verlag GmbH & Co. KGaA, Weinheim. (c) Schematic illustration of the EDL structures formed in the microfluidic capacitive sensors and the ion distribution in the microfluidic capacitive sensors along the microchannel. Reproduced with permission. Reproduced with permission.[197] Copyright The Royal Society of Chemistry 2017. (d) The triple-modal sensor and its circuit diagram. Reproduced with permission.[198] Copyright 2016 Wiley-VCH Verlag GmbH & Co. KGaA, Weinheim. (e) Schematic of the structure of the sensor for gas and physiological signal monitoring. Reproduced with permission.[199] Copyright 2018 American Chemical Society. (f) Preparation process of the multi-modal sensor that can respond to pressure, strain, temperature, and humidity. Reproduced with permission.[200] Copyright 2019 American Chemical Society.

sensor has been proposed that responds to pressure and temperature *via* capacitance and resistance changes, respectively. A pressure sensor based on the capacitive sensing mechanism reliant on the change in the hierarchical contact area of a surface-wrinkled pyramidal microstructure showed linear and high sensitivity. Meanwhile, for the temperature detection component, a non-physically contacting thermistor made from rGO was constructed. This thermistor exhibited nearly linear temperature sensitivity and posed no interference with the pressure readings. Humidity is another parameter that should be maintained within a specific range in the living environment to meet human comfort and requirements.[197]

Humidity sensing is also important for electronics because the high humidity leads to corrosion and even short circuits in electronic components, which significantly affects the performance of the devices.[201] Therefore, the e-skin is desirable to respond to humidity along with pressure and temperature. For this purpose, Miao *et al.* design a bi-functional humidity and pressure sensor based on CNT–polydimethylsiloxane (CNT–PDMS). The duration of ultraviolet, ozone treatment, and concentration of CNTs control the property of humidity sensing, while CNT concentration and grinding period of sugar granules were effective to control the pressure sensing. The sensors were able to effectively detect the humidity

changes of the surrounding environment and issued a warning when a hand approaches it. On touching the surface, the sensor could perceive the pressure and subsequently issued a contact warning. In addition, the sensor could also be affixed to the knee joint or a mask for tracking the human body movement status and the exhaled water molecules, respectively. This guidance can support individuals in pursuing scientifically sound and healthy exercise routines.[192] Utilizing the advantage of the humidity-sensitive ionic conductivity of a paper, a dual model pressure humidity sensor was fabricated by combining polyimide (PI)/paper and direct laser writing method, which converts the PI into a piezoresistive graphitic nanoplatelets structure.[202]

The nanocarbons can be utilized for both serving as electrodes and humidity sensing layers. A dual functional sensor with bioinspired multilayer 3D internal structure was designed to mimic the skin. Polyaniline-acidified MWCNTs composites (P–M) served as the conductive material, while the basal and piezoelectric layers were created by incorporating P–M into various layers of collagen aggregates (CA). Among them, piezoelectric layers function as external pressure sensors, whereas the basal layer serves as both cross electrodes and humidity sensing.[203] Humans possess a highly sensitive sense of smell, allowing them to perceive harmful gases in their surrounding environment. Medical and various industries also demand the detection of the environmentally harmful and human exhaled gases. Additionally, in humans, the exhalation of volatile organic compounds (VOCs) causes specific diseases.[204] This inspires the need for e-skin to incorporate olfactory functionality. A pressure/strain-gas dual model sensor was developed with carbon fiber based on triboelectric and gas-sensitive coupling mechanism. The device could actively detect VOCs in the atmosphere and human movements including finger touch, joint bending, and skin stretching.[205]

The incorporation of pressure/strain-gas sensors discussed above enables e-skin with the ability to perform olfactory as well as tactile sensing. To enhance and diversify the capabilities of e-skin, surface functional groups such as carboxyl, hydroxyl, and epoxy groups of rGO and GO are sensitive to the temperature and humidity in the environment. These functional groups play a significant role in enabling multifunctional sensing. Therefore, a triple model humidity–temperature–pressure sensors based all-graphene e-skin matrix was developed using a simple lamination process. The design of the sensor involved the growth of four graphene subelectrodes and two graphene main electrodes using CVD, which were subsequently transferred onto a PDMS substrate to create electrodes and interconnections. GO and rGO were sprayed onto two PDMS substrates to form humidity and temperature sensing layers with an identical structure. The top PDMS substrate was placed between two graphene electrodes, which was skilfully used as the sensing layer for the capacitive strain sensor. The circuit diagram of the prepared sensor is demonstrated in Fig. 15d. Each sensor in the e-skin matrix is responsible for the specific stimulation and remains unresponsive to the other two stimuli.[198] Another dual model sensor was developed to detect different gases in VOCs and physiological signals by processing rGO in two distinct manners. The upper layer of the sensor was utilized to detect various gases in the mixture, while the lower layer consisting of a porous rGO film to detect physiological signals was created using nanoparticles as a template. To avoid the overlap of signals, a polyimide film was introduced between two sensing layers, as displayed in Fig. 15e.[199]

A triple functional strain/pressure–temperature–humidity sensor was developed by the surface doping of a highly durable and continuous coating of graphene nanoplatelets on the surface of silicone rubber.[206] In order to achieve multimode e-skin, Liu *et al.* prepared a paper-based sensor to monitor pressure, temperature, strain, and humidity mas demonstrated in Fig. 15f.[200] The CB and rGO dispersion were sprayed on the paper substrate to fabricate a sensor. The sprayed rGO forms a uniform layer, whereas CB particles were absorbed within the cracks, and they overlap together to form a hierarchical structure. The developed unique structure was found to be impressively sensitive to multiple stimuli like pressure, strain, temperature, humidity, as well as human physiological signals. Notably, it could degrade in water without causing electronic pollutants.[200,207]

5. Working mechanism

Nanocarbon-based strain sensors represent a promising platform to monitor structural health, especially for smart biocomposites. These strain sensors detect and quantify mechanical strain by changes in the electrical or capacitive properties of carbon nanomaterials on mechanical deformation.[54,103] The choice of a specific carbon nanomaterial and sensor design depends on the desired sensitivity, response time, and application requirements. Based on their operating mechanisms, strain sensors are categorized into resistive, capacitive, and piezoelectric sensors. Out of them, piezoelectric strain sensors are composed of piezoelectric materials, which have the ability to convert mechanical pressure to electric potential.[102] Although, these sensors show high sensitivity and rapid response, their lack of flexibility and stretchability restrict their utilization in low strain range (less than 5% of strain). Therefore, these sensors are less explored; only few reports have been found on the utilization of these sensors for monitoring physiological signals.[158–160] The capacitive sensing mechanism relies on the change in capacitance when stress is applied. This change in capacitance occurs due to variations in the active surface area caused by shear forces and adjustments in the gap between electrodes resulting from perpendicular forces.[160] However, the sensitivity of the capacitive pressure sensor depends on the active area, and it diminishes rapidly as the device size is reduced.[159] The mechanism of piezoresistive pressure sensors based on a significant change in contact resistance extends beyond the intrinsic resistance, when pressure is applied. The intrinsic resistance undergoes changes due to a shift in the band structure during the defor-

mation of carbon-based nanomaterials. Most contact piezoresistive sensors display negative resistive outcomes, characterized by a decrease in resistance as the pressure increases.[125]

5.1 Nanocarbon-based strain sensors for structure deformation monitoring

Nanocarbons strain sensors utilized the unique properties of carbon-based nanomaterials, to detect mechanical strain through the deformation of their physical structure. The main principle behind nanocarbons strain sensors is the ability of nanocarbons to change their electrical, mechanical, or optical properties in response to mechanical deformation.[208] Understanding the working mechanisms is essential for harnessing their potential in SHM. The strain sensors, composed of whisker carbon nanotubes (WCNT), causes the deformation of conductive networks formed by these nanotubes, which are highly sensitive to external mechanical stimuli. This structural deformation can lead to a change in the count of effective electron paths, which causes a change in the electric resistance of CNT networks. Fig. 16a represents the schematic illustration of the deformation process of WCNT as it undergoes stretching and subsequent release.[209] Fig. 16b and c display the SEM images of WCNT film during both the stretching and releasing phases.[209] Fig. 16d shows the photograph of structural deformation under displacement, which is corresponding to Poisson's negative ratio.[209] For a better understanding of the structural deformation behaviour, a hexagonal configuration was deliberately adopted in the mould to imprint its shape onto the moulded auxetic structure, as illustrated in Fig. 16e. The enhancement in strain in the longitudinal direction caused a rotation of these hexagons; further, this rotation causes the structure to increase its width in the transverse

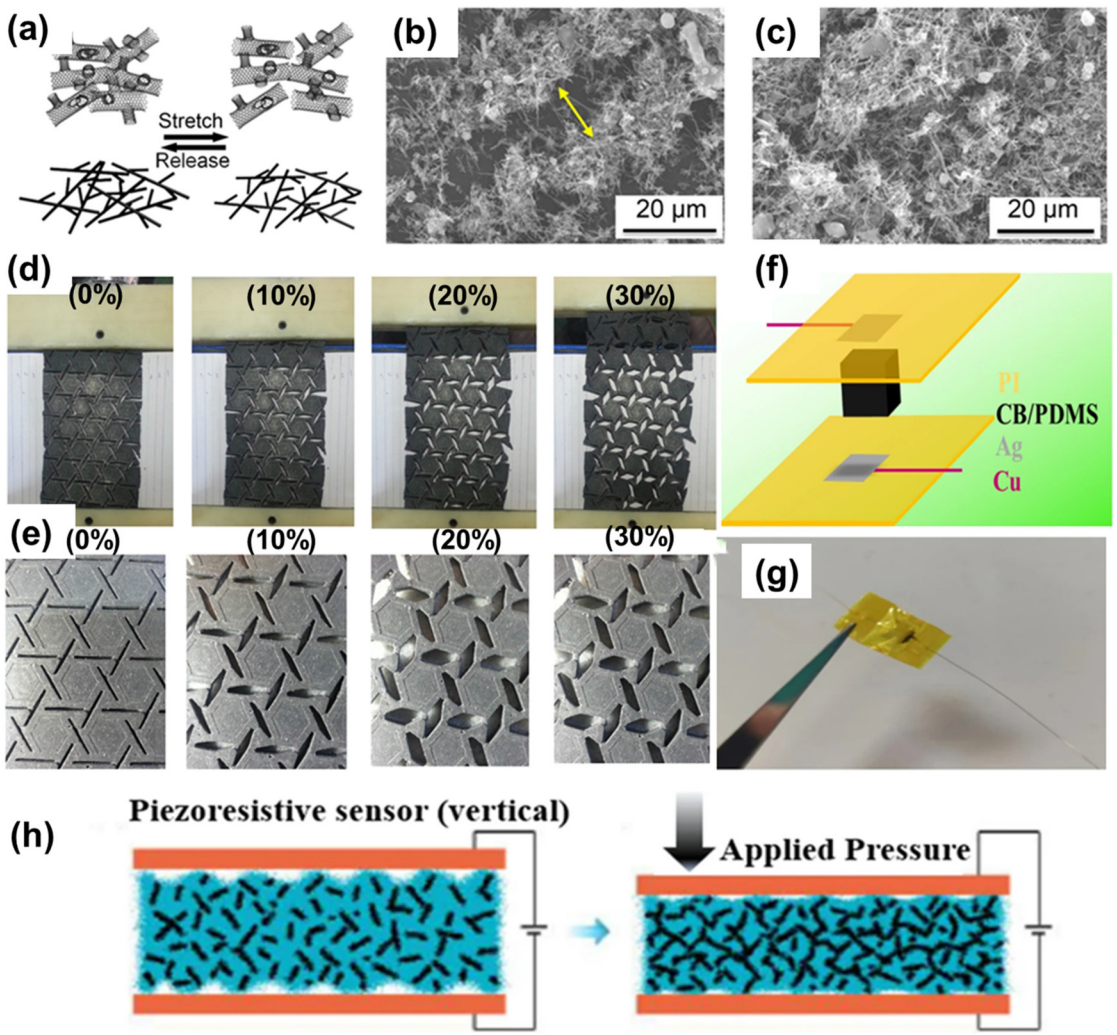

Fig. 16 (a) The schematic diagram of the deformation of the 3D networks of WCNT films during stretching and releasing. (b) The SEM image of WCNT films during stretching and (c) during release. (d) Sequence pictures of the suggested auxetic sensor deformation experimentally. Reproduced with permission.[209] Copyright 2021 Elsevier Ltd. (e) Deformation mechanism of the isotropic auxetic sensor with fixed Poisson's ratio. Reproduced with permission.[230] Copyright 2023 SAGE Publications (f) Schematic structure of flexible piezoresistive sensors. (g) Photograph of an as-assembled PDMS/CB sensor and (h) schematic illustration of sensing mechanisms of piezoresistive sensor with vertical electrode design. Reproduced with permission. Reproduced with permission.[210]

direction, and hence, the structure has a negative Poisson's ratio. Thus, the mechanism of deformation of the auxetic structure is the rotation of the hexagons inside the unit cell.[230]

CB-based (PDMS/CB) flexible piezoresistive sensors were assembled, as depicted in Fig. 16f, with an accompanying optical photograph, as shown in Fig. 16g.[210] These sensors monitored SHM by monitoring changes in the CB electrical conductive networks induced by material deformation under external mechanical pressure. The sensors experienced a reduction in both the bulk resistance of the sensing material (PDMS/CB) itself and the contact resistance between the porous PDMS/CB composite materials and the electrodes under pressure loading. As a result, the output current increases when the device is powered by a constant voltage. The proposed mechanism of prepared sensor is illustrated in Fig. 16h.[210]

Fig. 17 represents the schematic illustration of strain sensing mechanism of the composites with various conductive networks.[211] The CB/elastic band (EB) composite conductive network was formed by a large number of contact points between CB particles. However, these contact points were not closely connected and susceptible to fracture when subjected

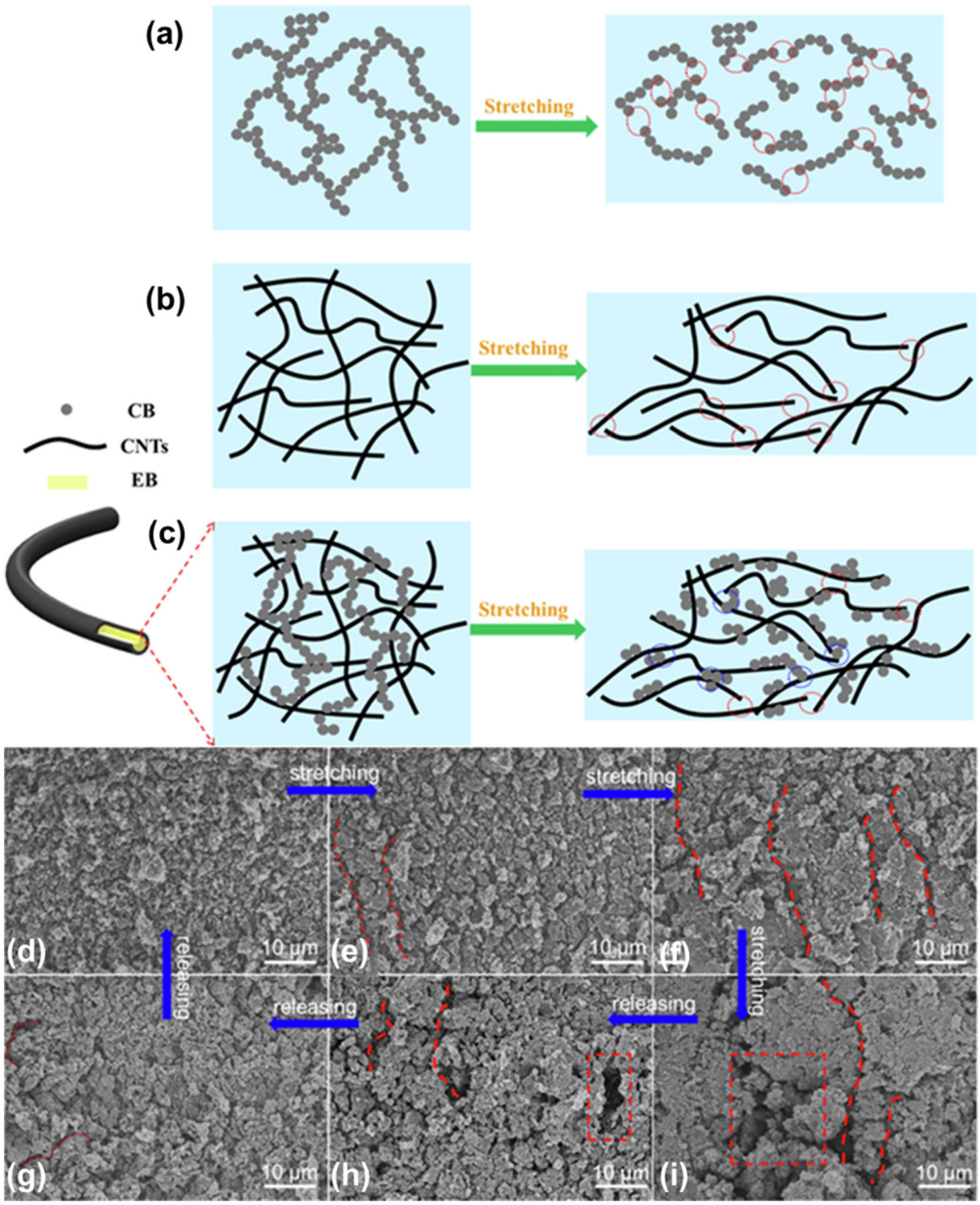

Fig. 17 Schematic diagram of the strain sensing mechanisms of the composites with different conductive networks. (a) CB–EB; (b) CNTs–EB; (c) (CB + CNTs)–EB and SEM surface morphologies of the PDMS/(CB + CNTs)/EB composite strain sensor at different stretching and releasing status. (d) 0%; (e) 50%; (f) 100%; (g) 200%; (h) 100%; (i) 50%. Reproduced with permission.[211] Copyright 2022 Elsevier Inc.

to strain. As a result, the CB conductive network showed high sensitivity to stretching (Fig. 17a). On the other hand, in CNTs/EB composites, due to a large aspect ratio of CNTs, there are lower number of contact points between them, as demonstrated in Fig. 17b. Moreover, the interweaving of CNTs makes a more stable conductive network as compared to CB. Therefore, the CB conductive network showed higher strain sensitivity than CNTs conductive network. In addition, during the release process, the CB network restored the initial position while it was difficult to rebuild the damaged conducting network for CNTs. Conversely, the larger aspect ratio and their greater facilitation of conductive networks formation of CNTs enhanced the conductivity of polymer network more than CB. Achieving a similar conductivity requires an increase in the loading of more CB nanoparticles in the polymer matrix, which leads to an increase in cost and complexity. Additionally, under high strain, CB-based networks can easily become completely disconnected, which results in the sensor's inability to function properly. Three distinct contact modes such as CNTs–CNTs, CB–CB, and CB–CNTs exist in the conducting network of CB–CNTs. It becomes clear that both CB–CB and CB–CNTs contacts exhibit superior recoverability during the stretching and releasing cycles as compared to CNTs–CNTs contacts. The incorporation of CB nanoparticles forms a denser conductive network for CNTs, which helps to repair broken connections by some CB particles potentially migrating into the gaps between CNTs. As illustrated in Fig. 17c, some permanent damages occur within the CNTs network (red circles), but some of these damaged connections are reformed with the assistance of CB nanoparticles (blue circles).[211] Consequently, the hybrid CB–CNTs conductive network, formed through the synergistic effects of CB and CNTs, integrates the strengths of both materials. This results in the (CB + CNTs)/EB composite sensors that offer the benefits of an extended strain range, higher sensitivity, and remarkable recoverability. Fig. 17(d–i) shows the microstructure evolution of the (CB + CNTs)/EB composite under various stretching and releasing states. The CB + CNTs mixture is closely connected on the surface of EB before stretching. As the applied strain increases, the size of cracks expands (as indicated by the red dashed line in Fig. 17e–g), leading to the disruption of the conductive pathway and a subsequent increase in resistance. When the strain reaches a critical threshold, the conductive network becomes entirely compromised, resulting in the formation of an open circuit. Upon releasing the applied strain, the process of network restoration commences, and the size of the cracks gradually decreases (Fig. 17h and i). When the tensile strain returns to zero, the conductive network can fully recover to its initial state (Fig. 17d), ensuring the sensor's robust repeatability and durability.[211]

5.2 Graphene strain sensors with over-connected graphene sheets

Graphene strain sensors with over-connected graphene sheets refer to a type of strain sensor in which graphene is used as the sensing material. In this context, "over-connected" likely means that the graphene sheets are structured in such a way that it enhances the connectivity between them, which can enhance the electrical conductivity in response to the strain. The larger sheet of the graphene is composed of smaller interconnected flakes. From a perspective at the nanoscale, the distortion in a small graphene flake may change the resistivity of the sheet, consequently modifying the resistance across the entire conducting system when subjected to mechanical strain.[212] The mechanism of graphene nanowall-based strain sensor for monitoring high intraocular pressure is illustrated in Fig. 18a.[213] As a nanofilm, graphene nanowalls attached with the contact lance were stretched in the synchronization. The graphene sheets in graphene nanowalls stretched separately with an increase in the intraocular pressure. As a result, the overall resistance of the device increased since the contact part between graphene nanowalls decreased. The SEM images in Fig. 18b–d demonstrate the formation of cracks with increasing stretching.[213] COMSOL simulations were also performed to investigate the working mechanism of strain sensors designed by the wrapping of graphene on a 3D printed substrate. The simulation was performed on a square cell in a porous structure under both pulls (Fig. 18e) and starched (Fig. 18f) conditions of cells. The side resistance (R_1) decreased on stretching the side because of the loss of conducting path. On the other hand, it increases on compressing the side because of the formation of more conducting path, as demonstrated in Fig. 18g.[214] Fig. 18h illustrates that the graphene sheet accumulating at the corner would be pulled apart on stretching the corners, which would reduce the corner resistance (R_2) while the sheet accumulating at the corner would be compressed on squeezing the corners (Fig. 18i).[214] The stretching direction compressed two corners, while the other two corners were stretched. Since the compression angle was equal to the stretching angle, this resulted in a negligible change in R_2. Consequently, the change in resistance mainly depends on the change in resistance R_1. Therefore, the simulation result shows that when the sensor was stretched, the edges of the pore stretch and expand in accordance with the graphene layer's operating principle, leading to an increase in resistance (R). Conversely, when pressure is applied to the sensor, the pore's edges stretch and compress, causing a reduction in R.[214]

The piezoresistive behaviour of graphene-based silk fabric sensors was found to be direction-dependent. This may be associated with the mechanical and structural properties of the silk fabric substrate in different orientations. Fig. 18j demonstrates that under the same strain level, higher stress is transferred along the 0° direction to the rGO layer because of the higher Young's modulus in this direction, resulting in more microcracks in the conducting layer.[215] In the case of sensors with elevated structure, the contact area changes when subjected to stress, causing changes in resistance. A laser-scribed graphene-created foam-like structure (Fig. 18k) with crossbar-based pressure sensing core consisting of face-to-face two laser-scribed graphene film (Fig. 18l) decreases its resis-

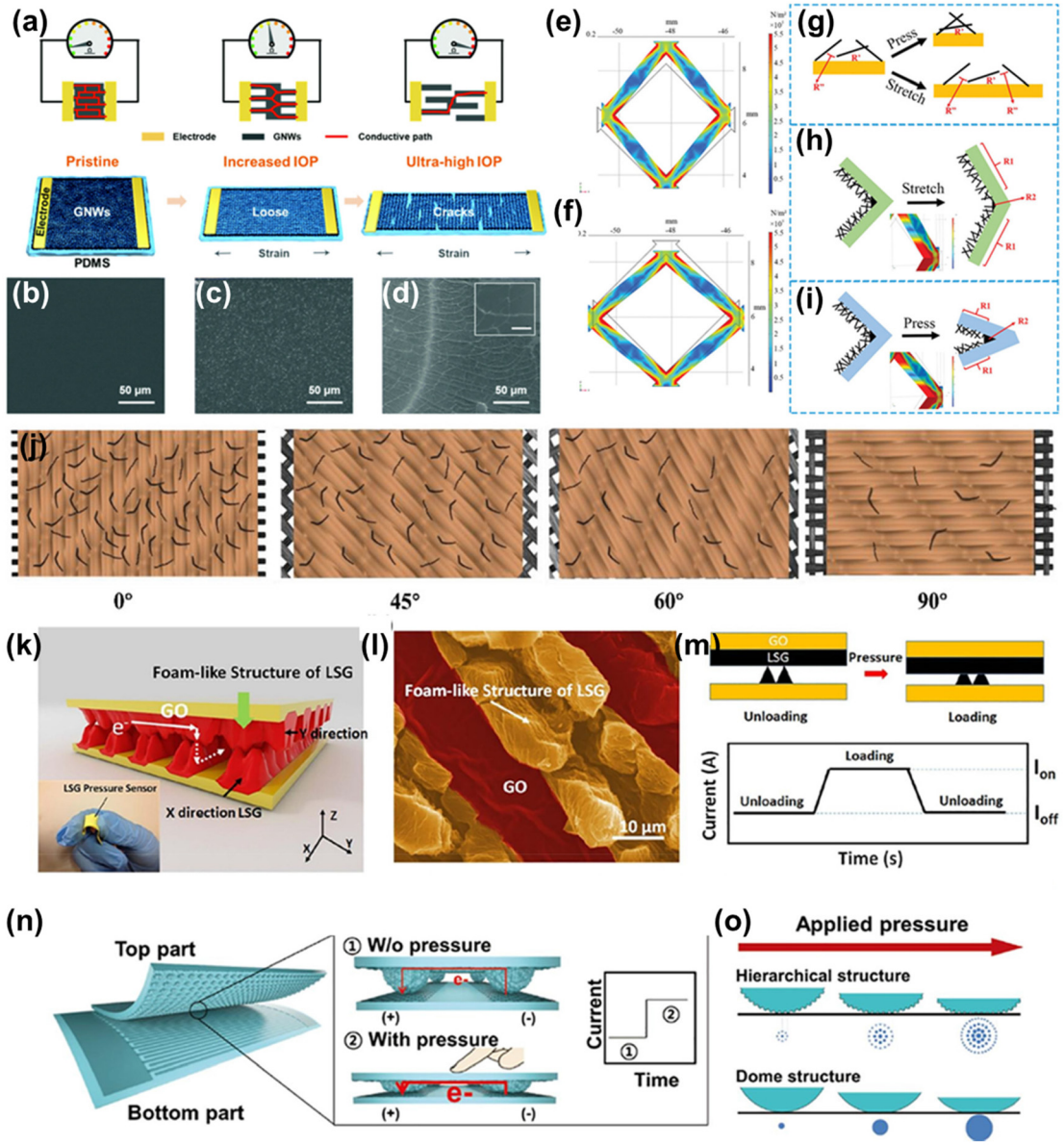

Fig. 18 (a) The resistance response mechanism of GNW/PDMS in GNW–CLS; the corresponding SEM images of (b) initial, (c) increased IOP, and (d) ultra-high IOP are shown at the bottom; the inset shows the local details of cracks. Reproduced with permission. Copyright The Royal Society of Chemistry 2020.[213] (e) The simulation of a square cell in the porous structure under stretching and (f) pressing, (g) working diagram of the graphene nanosheets layer. (h) Corner of the cell under stretching and (i) pressing. Reproduced with permission. Reproduced with permission.[214] Copyright 2021 Wiley-VCH GmbH. (j) Mechanism of the graphene-silk fabric strain sensor. Reproduced with permission. Reproduced with permission.[215] Copyright 2019 Wiley-VCH Verlag GmbH & Co. KGaA, Weinheim. (k) Cross-bar device structure of the pressure sensor based on the foam-like laser-scribed graphene sensor (inset shows the image of the pressure sensor). (l) Top view SEM image of the LSG. (m) Working mechanism of foam-like laser-scribed graphene sensor. Reproduced with permission. Reproduced with permission.[216] (n) Schematic illustration of sensor assembly and operating principle of the pressure sensor composed of the hierarchical graphene/PDMS array. (o) An illustration that shows the effects of the hierarchical structure. Reproduced with permission.[217] Copyright 2016 Wiley-VCH Verlag GmbH & Co. KGaA, Weinheim.

tance on applying pressure, resulting in increasing the current through the device, as demonstrated in Fig. 18m.[216] Another sensor based on a similar working mechanism was developed using bioinspired hierarchical structure consisting of PDMS covered with a monolayer of graphene, as shown in Fig. 18n. The hierarchical structure makes this sensor dominant from the traditional protuberance structure by ensuring the autonomy of each individual small protuberance (Fig. 18o).[217] As the pressure increases, a number of small protuberances in contact linearly increases, which results in a proportional increase in the contact area. This effectively eliminates the nonlinearity issue as seen in traditional dome structures and contributes to generate novel graphene-based strain sensors.[217]

The incorporation of metal nanoparticles in the graphene structure significantly enhances the performance of strain sensors. An innovative piezoresistive sensor was developed using rGO and Ag nanowires incorporated into cotton fiber films in which the electrodes were connected to the rGO side. Consequently, charge transfer exclusively occurs between face-to-face orientated rGO sheets without sensing any stress, resulting in a state of high resistance. On the other hand, the introduction of stress brings the Ag nanowire-based cotton fiber film into close contact with the rGO-based cotton fiber film, created much faster pathways for charge transfer, thus resulted in a low resistance state.[218] Furthermore, the incorporation of $Pt(acac)_2$ in the homogeneous laser-induced graphene (LIG) generates lump-like structures in the LIG network. Fig. 19(a) shows the homogeneous structure of LIG without Pt $(acac)_2$ additive incorporation.[219] The SEM images in Fig. 19b–d demonstrate the structure change of LIG network with different Pt loadings. The structural changes of the homogeneous LIG network involved the gradual disconnection of the conductive pathways among graphene flakes, from the initial state at a low strain to the high-strain state, as depicted in Fig. 19e.[219] The addition of $Pt(acac)_2$ enhanced the gauge

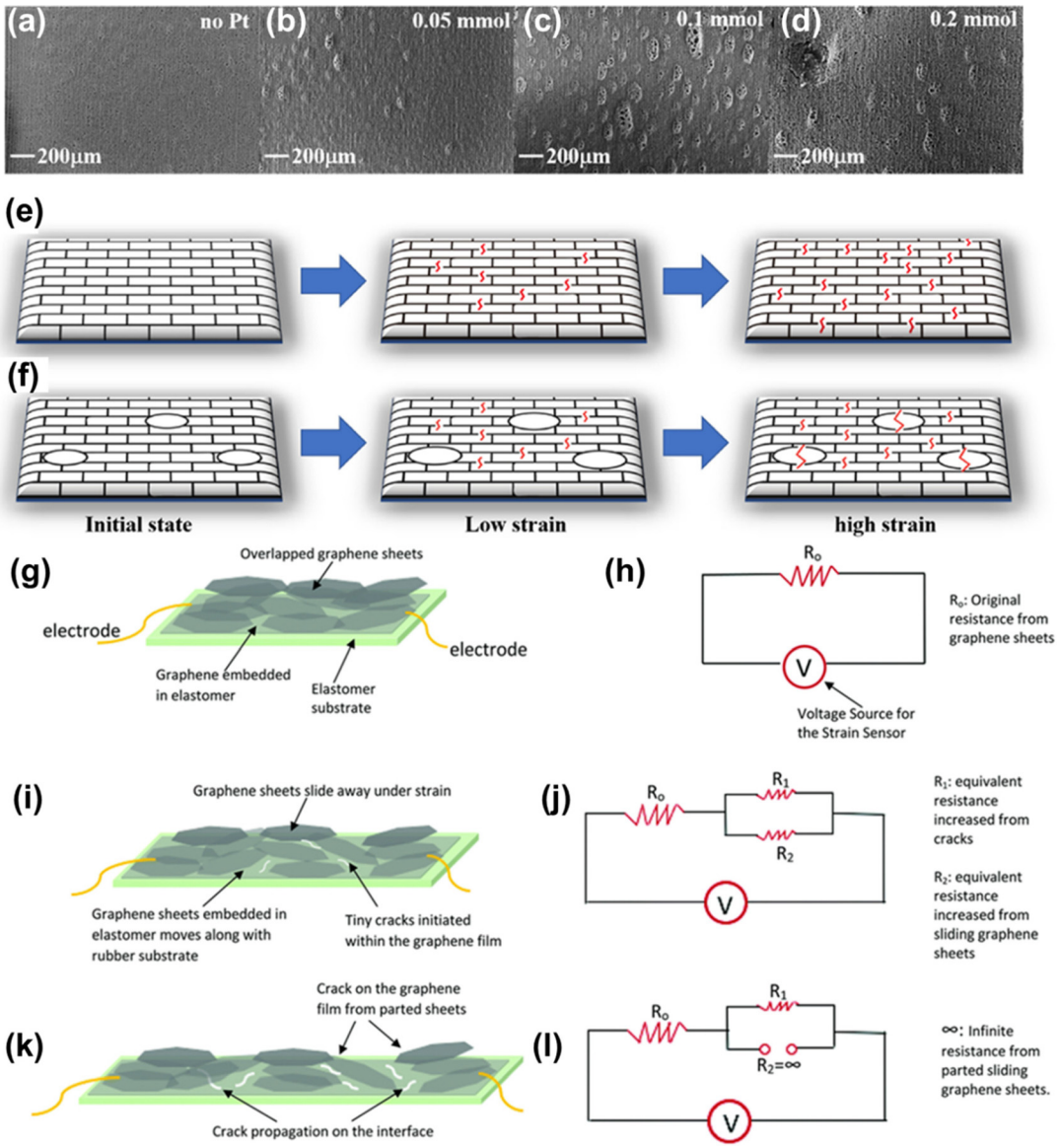

Fig. 19 (a) FESEM images of direct laser writing on PBI/$Pt(acac)_2$ film: no $Pt(acac)_2$, (b) 0.05 mmol, (c) 0.1 mmol, (d) 0.2 mmol; diagrams showing the sensing mechanism of the device: (e) without $Pt(acac)_2$, (f) with $Pt(acac)_2$. Reproduced with permission. Reproduced with permission.[219] Copyright 2022 Elsevier Ltd. (g) Graphene film on substrate, (h) equivalent electrical circuit when a sensor is in an undeformed state, (i) movement of graphene under small strain, (j) equivalent electrical circuit when the sensor under small strain, (k) movement of graphene under large strain, and (l) equivalent electrical circuit when the sensor is under large strain. Reproduced with permission.[220] Copyright The Royal Society of Chemistry 2020.

factor at a high strain; therefore, these lump-like structures were found to exhibit more pronounced electrical disconnections and played an important role in the distraction of conductive pathways at high strain (Fig. 19f).[219]

The calibration of conventional stretchable sensors is a great challenge because of the occurrence of various sensitivity curves in certain linear zones characterized by various gauge factors. A stretchable and well-calibrated sensor was fabricated by placing a patterned graphene film onto an elastomer sheet, as indicated in Fig. 19g.[220] The electronic circuit under constructed sensor is shown in Fig. 19h.[220] Under strain less than 2%, small number of microcracks were generated at the inter-

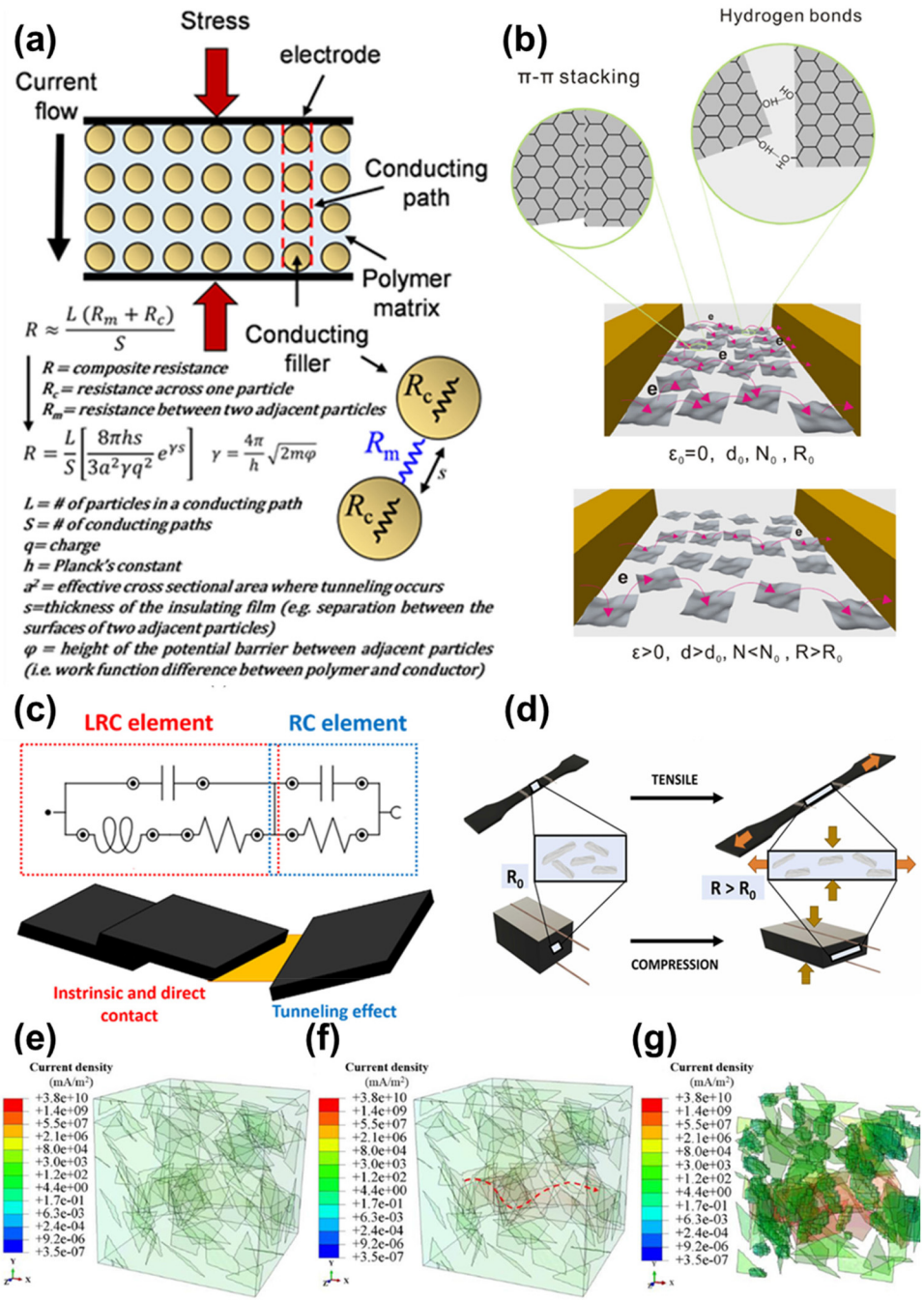

Fig. 20 (a) Schematic representation of the tunnelling mechanism. Reproduced with permission.[221] (b) Tunnelling and destruction mechanism of graphene quantum dot-based strain sensors. Reproduced with permission.[223] Copyright 2022 The Authors. Published by Elsevier Ltd. (c) Series–parallel LRC–RC circuit for graphene nanoplatelet-based sensor. Reproduced with permission.[224] (d) Schematics of the mechanism of the sensors under tensile and compression conditions. Reproduced with permission.[225] Current density distribution of graphene rubber composites. (e) Neglecting the tunnelling effect, (f) considering the tunnelling effect, (g) conductive paths formed in the graphene rubber composites. Reproduced with permission.[226] Copyright 2020 Elsevier Ltd.

face of graphene film and substrate; also, the relative sliding between the graphene sheets (unembedded in the substrate) takes place inside the film (Fig. 19(i)).[220] The equivalent circuit diagram is represented in Fig. 19j.[220] Beyond a strain level of 32% (Fig. 19(k)), the sensing primarily depends only on the propagating cracks as the connection between sliding graphene sheets starts losing contact with each other. The respective electronic circuit diagram is depicted in Fig. 19(l).[220]

5.3 Graphene strain sensors based on the tunnelling effect between neighbouring graphene sheets

Graphene strain sensors based on the tunnelling effect utilize the unique electrical properties allow them to function as highly sensitive and responsive sensors for measuring the mechanical strain. The tunnelling effect in graphene-based sensors refers to the tunnelling of electrons through the barrier formed by the potential energy difference between narrow spaced layers of graphene. The resistance of the sensor depends on the separation between the layers of graphene. The high gauge factor can be achieved using this mechanism in strain sensors composed of graphene. According to the tunnelling mechanism, by considering the matrix resistance constant and ignoring the resistance normal to the direction of current flow, the overall resistance of the sensor depends on the count of particles between the electrodes and the number of conducting pathways, as demonstrated in Fig. 20a.[221,222] The graphene quantum dot-based strain sensors also follow a similar mechanism. Fig. 20b shows that on stretching the sensor, the tunnelling distance between graphene quantum dots increases ($d > d_0$), while the count of conduction pathways decreases ($d > d_0$). Thus, the overall resistance of the device increases.[223]

The mechanism for the AC electrical response of graphene nanoplatelets reinforced PDMS-based strain sensors have also been explored. The electrical network can be modelled as a combination of a series–parallel circuit consisting of both RC (resistor–capacitor) and LRC (inductor–resistor–capacitor) elements (Fig. 20c).[224] The RC network is corresponding to the tunnelling effect taking place between neighbouring nanoparticles while the LRC element represents the intrinsic resistance and contact resistance. This model was found to be consistent with the experimentally obtained data.[224] Similarly, graphene nanoplatelets incorporated with Ecoflex-based strain sensors also follow the linear–exponential behaviour of resistance representing the tunnelling effect between the neighbourhood graphene nanoplatelets. Moreover, as the concentration of graphene nanoplatelets decreases, the gauge factor increases. This is because of the variation of the tunnelling distance between adjacent graphene nanoplatelets. In this study the electrical resistance does not decrease initially since it follows the out-of-plane mechanism, which leads to an increase in the resistance because of the Poisson effect, as indicated in Fig. 20d.[225] In order to find the role of tunnelling effect in graphene-based strain sensors more accurately, a representative model of graphene rubber element was analyzed. In this model, the random and uniform distribution of graphene was considered; the current density of the rubber matrix was found to be minimal in the composite. Thus, the composite was insulated in the absence of the tunnelling effect (Fig. 20e), whereas on considering the tunnelling effect, the current density of the composite was increased about 10^6 times than that of the previous case (Fig. 20f).[226] Moreover, the number of conducting paths were more prominent through the tunnelling process when the distance function $s(x)$ was less than 3 nm in the distribution of graphene sheets within the rubber matrix in the representative volume element model (Fig. 20g). In conclusion, the tunnelling effect plays an important role in the prediction of the conductivity of graphene polymer composites.[226]

6. Conclusion and future prospective

In conclusion, nanocarbon-based sensors for SHM of smart biocomposite involve leveraging cutting-edge nanotechnology to improve the performance, consistency, and sustainability of composite materials used in different structural applications. Nanocarbons provide exceptional sensitivity to detect even subtle changes as well as enable the monitoring of multiple parameters such as strain, temperature, and humidity, providing a comprehensive understanding of the composite's health in the structural integrity of biocomposites. Additionally, nanocarbons facilitate the real-time monitoring and allow the immediate detection and responses to structural changes, which ensure optimal performance and longevity of smart biocomposite.

Overall, in the present scenario, much progress has been made on nanocarbon-based sensing systems for various applications in smart biocomposites, such as damage detection, strain sensing, monitoring of failure, determination of mechanical strength, and pressure sensing. Nevertheless, in the future, many challenges continue to be addressed, and recent developments can be detailed. The fabrication procedure, functionalization, and heteroatoms doping have a pronounced effect on their sensing properties. So far, the exact tailoring of the well-defined structures and morphologies of nanocarbons remains a challenging task. Furthermore, manufacturing processes for nanocarbon-based strain sensors can be precise and complex, which can pose challenges in large-scale production. Some nanocarbons may be sensitive to environmental conditions, such as humidity and temperature, which can affect their performance and reliability. Moreover, the long-term performance and accuracy of sensors can also be affected by the degradation of the properties of nanocarbons over time. The lack of standardized testing and calibration procedures for these strain sensors can pose challenges in ensuring reliability and comparability across different devices. Integrating nanocarbon-based sensors into existing smart biocomposite structures may require specialized expertise and pose integration challenges in certain applications.

Several critical issues before the widespread adaptation of smart composites need to be addressed including the relationship between physiochemical characteristic and techno-economic analysis as well as related environmental risk. A comprehensive understanding of the microstructural and chemical and reactivity difference among various nanocarbons and their derivatives, especially nanocarbons synthesized from traditional techniques and biomass-derived nanocarbons, is limited. A clear relationship between the type of nanocarbons and electrical properties, sensing properties, and piezo-resistive properties remains elusive.

Conflicts of interest

There are no conflicts to declare.

Acknowledgements

KMT acknowledges financial assistance from the Department of Biotechnology (DBT), India, through the Ramalingaswami Faculty Award (BT/RLF/Re-entry/45/2018).

References

1 M. Z. R. Khan and S. Srivastava, *IOP Conf. Ser.: Mater. Sci. Eng.*, 2018, **404**, 012028.
2 M. S. Dharek, J. Vengala, P. Sunagar, K. Sreekeshava, P. Kilabanur and P. Thejaswi, *Smart Technologies for Energy, Environment and Sustainable Development*, 2022, vol. 1, pp. 151–165.
3 S. Malekmohammadi, N. Sedghi Aminabad, A. Sabzi, A. Zarebkohan, M. Razavi, M. Vosough, M. Bodaghi and H. Maleki, *Biomedicines*, 2021, **9**, 1537.
4 M. T.-u. Safian, K. Umar, T. Parveen, A. A. Yaqoob and M. N. M. Ibrahim, *Smart Polymer Nanocomposites*, Elsevier, 2021, pp. 183–204.
5 T. Altalhi, *Handbook of bioplastics and biocomposites engineering applications*, John Wiley & Sons, 2022.
6 A. Biswal and S. K. Swain, *Polymer nanocomposite-based smart materials*, Elsevier, 2020, pp. 197–210.
7 A. A. Basheer, *Aircr. Eng. Aerosp. Technol.*, 2020, **92**, 1027–1035.
8 R. Min, Z. Liu, L. Pereira, C. Yang, Q. Sui and C. Marques, *Opt. Laser Technol.*, 2021, **140**, 107082.
9 V. Rahul, S. Alokita, K. Jayakrishna, V. Kar, M. Rajesh, S. Thirumalini and M. Manikandan, *Structural health monitoring of biocomposites, fibre-reinforced composites and hybrid composites*, Elsevier, 2019, pp. 33–52.
10 D. J. Inman, C. R. Farrar, V. L. Junior and V. S. Junior, *Damage prognosis: for aerospace, civil and mechanical systems*, John Wiley & Sons, 2005.
11 W. Staszewski and K. Worden, *Health monitoring of aerospace structures*, 2004, p. 163.
12 C. R. Farrar and K. Worden, *Philos. Trans. R. Soc., A*, 2007, **365**, 303–315.
13 A. Negi, *Math. Stat. Eng. Appl.*, 2021, **70**, 698–705.
14 S. S. Saidin, A. Jamadin, S. Abdul Kudus, N. Mohd Amin and M. A. Anuar, *Int. J. Concr. Struct. Mater.*, 2022, **16**, 1–17.
15 T. Harms, S. Sedigh and F. Bastianini, *IEEE Instrum. Meas. Mag.*, 2010, **13**, 14–18.
16 S. Hui, L. Charlebois and C. Sun, *Can. J. Earth Sci.*, 2018, **55**, 221–229.
17 C. Scuro, F. Lamonaca, S. Porzio, G. Milani and R. Olivito, *Constr. Build. Mater.*, 2021, **290**, 123092.
18 P. Kot, M. Muradov, M. Gkantou, G. S. Kamaris, K. Hashim and D. Yeboah, *Appl. Sci.*, 2021, **11**, 2750.
19 P. Gardner, R. Fuentes, N. Dervilis, C. Mineo, S. Pierce, E. Cross and K. Worden, *Philos. Trans. R. Soc., A*, 2020, **378**, 20190581.
20 T. N. Tallman and D. J. Smyl, *Smart Mater. Struct.*, 2020, **29**, 123001.
21 B. Han, S. Ding and X. Yu, *Measurement*, 2015, **59**, 110–128.
22 S. Rana, R. Fangueiro and A. G. Correia, *AIMS Mater. Sci.*, 2016, **3**, 357–379.
23 S. Sony, S. Laventure and A. Sadhu, *Struct. Control Health Monit.*, 2019, **26**, e2321.
24 M. Abdulkarem, K. Samsudin, F. Z. Rokhani and M. F. A. Rasid, *Struct. Health Monit.*, 2020, **19**, 693–735.
25 A. Di Graziano, V. Marchetta and S. Cafiso, *J. Traffic Transp. Eng.*, 2020, **7**, 639–651.
26 L. Su, X. Yu, K. Li and M. Pecht, *Microelectron. Reliab.*, 2020, **110**, 113657.
27 J. S. Chilles, A. F. Koutsomitopoulou, A. J. Croxford and I. P. Bond, *Compos. Sci. Technol.*, 2016, **134**, 81–88.
28 V. Giurgiutiu, *Structural health monitoring of aerospace composites*, Academic Press, 2015.
29 M. Hrovat, D. Belavič and Z. Samardžija, *J. Eur. Ceram. Soc.*, 2001, **21**, 2001–2004.
30 A. A. Barlian, W.-T. Park, J. R. Mallon, A. J. Rastegar and B. L. Pruitt, *Proc. IEEE*, 2009, **97**, 513–552.
31 H. Rocha, C. Semprimoschnig and J. P. Nunes, *Eng. Struct.*, 2021, **237**, 112231.
32 J. Qin, L. J. Yin, Y. N. Hao, S. L. Zhong, D. L. Zhang, K. Bi, Y. X. Zhang, Y. Zhao and Z. M. Dang, *Adv. Mater.*, 2021, **33**, 2008267.
33 P. Jiao, K.-J. I. Egbe, Y. Xie, A. Matin Nazar and A. H. Alavi, *Sensors*, 2020, **20**, 3730.
34 L. Ma, W. Qiu and X. Fan, *Microelectron. Reliab.*, 2021, **118**, 114045.
35 F. Wang, J. Jiang, Q. Liu, Y. Zhang, J. Wang, S. Wang, L. Han, H. Liu and Y. Sang, *Nano Energy*, 2020, **70**, 104457.
36 Y. Shen, W. Yang, F. Hu, X. Zheng, Y. Zheng, H. Liu, H. Algadi and K. Chen, *Adv. Compos. Hybrid Mater.*, 2023, **6**, 21.
37 J. Chen, J. Zhu, Z. Wei, Z. Chen, C. Zhu, Q. Gao and C. Gao, *J. Mater. Chem. C*, 2023, **11**, 13358–13369.

38 M. Zhang, W. Yang, Z. Wang, H. Liu, R. Yin, C. Liu and C. Shen, *Appl. Phys. Lett.*, 2023, **122**, 043507.
39 C. Sun, J. Zhang, Y. Zhang, F. Zhao, J. Xie, Z. Liu, J. Zhuang, N. Zhang, W. Ren and Z.-G. Ye, *Appl. Surf. Sci.*, 2021, **562**, 150126.
40 R. Nur, N. Matsuhisa, Z. Jiang, M. O. G. Nayeem, T. Yokota and T. Someya, *Nano Lett.*, 2018, **18**, 5610–5617.
41 S.-R. Kim, J.-H. Kim and J.-W. Park, *ACS Appl. Mater. Interfaces*, 2017, **9**, 26407–26416.
42 H. Souri, J. Yu, H. Jeon, J. W. Kim, C.-M. Yang, N.-H. You and B. Yang, *Carbon*, 2017, **120**, 427–437.
43 H. Souri, I. W. Nam and H.-K. Lee, *Compos. Sci. Technol.*, 2015, **121**, 41–48.
44 M. Amjadi, M. Turan, C. P. Clementson and M. Sitti, *ACS Appl. Mater. Interfaces*, 2016, **8**, 5618–5626.
45 M. Amjadi, Y. J. Yoon and I. Park, *Nanotechnology*, 2015, **26**, 375501.
46 X. Zhang, N. Zhao and C. He, *Prog. Mater. Sci.*, 2020, **113**, 100672.
47 M. Li and B. Mu, *Appl. Energy*, 2019, **242**, 695–715.
48 Y. Fang, Y. Liu, L. Qi, Y. Xue and Y. Li, *Chem. Soc. Rev.*, 2022, **51**, 2681–2709.
49 G. Yang, L. Liu and Z. Wu, *Smart Mater. Struct.*, 2019, **28**, 065009.
50 A. Hussain, Y. Xiang, T. Yu and F. Zou, *Constr. Build. Mater.*, 2022, **359**, 129496.
51 H. Li, J. Chen, X. Chang, Y. Xu, G. Zhao, Y. Zhu and Y. Li, *J. Mater. Chem. A*, 2021, **9**, 1795–1802.
52 P. Kumari, K. M. Tripathi, K. Awasthi and R. Gupta, *Ind. Eng. Chem. Res.*, 2023, **62**, 13837–13847.
53 R. Aggarwal, S. K. Sonkar and K. M. Tripathi, *Carbon*, 2023, **208**, 436–442.
54 T. T. Tung, M. Moussa, K. M. Tripathi, T. Kim, M. J. Nine, A. K. Nanjundan, D. Dubal and D. Losic, *Sustainable Mater. Technol.*, 2022, **32**, e00393.
55 M. Amjadi, K. U. Kyung, I. Park and M. Sitti, *Adv. Funct. Mater.*, 2016, **26**, 1678–1698.
56 A. Nag, M. E. E. Alahi, S. C. Mukhopadhyay and Z. Liu, *Sensors*, 2021, **21**, 1261.
57 L. Liu and D. Zhang, *Composites, Part A*, 2015, **75**, 46–53.
58 S. Luo and T. Liu, *Adv. Mater.*, 2013, **25**, 5650–5657.
59 Z. Wang, Y. Huang, J. Sun, Y. Huang, H. Hu, R. Jiang, W. Gai, G. Li and C. Zhi, *ACS Appl. Mater. Interfaces*, 2016, **8**, 24837–24843.
60 J. Lee, S. Shin, S. Lee, J. Song, S. Kang, H. Han, S. Kim, S. Kim, J. Seo and D. Kim, *ACS Nano*, 2018, **12**, 4259–4268.
61 B. Hao, L. Mu, Q. Ma, S. Yang and P.-C. Ma, *Compos. Sci. Technol.*, 2018, **163**, 162–170.
62 Q. Wang, M. Jian, C. Wang and Y. Zhang, *Adv. Funct. Mater.*, 2017, **27**, 1605657.
63 I. Kang, M. J. Schulz, J. H. Kim, V. Shanov and D. Shi, *Smart Mater. Struct.*, 2006, **15**, 737.
64 J. Wang, H. Liu, X. Yue, D. Zhang, R. Yin, H. Sun, C. Liu and C. Shen, *Mater. Today Nano*, 2023, **24**, 100427.
65 S. Zhang, K. Sun, H. Liu, X. Chen, Y. Zheng, X. Shi, D. Zhang, L. Mi, C. Liu and C. Shen, *Chem. Eng. J.*, 2020, **387**, 124045.
66 H. Sun, Y. Bu, H. Liu, J. Wang, W. Yang, Q. Li, Z. Guo, C. Liu and C. Shen, *Sci. Bull.*, 2022, **67**, 1669–1678.
67 S. Yang, W. Yang, R. Yin, H. Liu, H. Sun, C. Pan, C. Liu and C. Shen, *Chem. Eng. J.*, 2023, **453**, 139716.
68 Y. Shen, *Fuel Process. Technol.*, 2022, **236**, 107437.
69 M. Gao, C.-C. Shih, S.-Y. Pan, C.-C. Chueh and W.-C. Chen, *J. Mater. Chem. A*, 2018, **6**, 20546–20563.
70 S. K. Tiwari, M. Bystrzejewski, A. De Adhikari, A. Huczko and N. Wang, *Prog. Energy Combust. Sci.*, 2022, **92**, 101023.
71 A. Sharma, R. K. Sharma, Y.-K. Kim, H.-J. Lee and K. M. Tripathi, *J. Environ. Chem. Eng.*, 2021, **9**, 106656.
72 M. Park, A. Sharma, C. Kang, J. Han, K. M. Tripathi and H.-J. Lee, *ACS Biomater. Sci. Eng.*, 2022, **8**, 2131–2141.
73 P. Kumari, K. M. Tripathi, K. Awasthi and R. Gupta, *Environ. Sci. Pollut. Res.*, 2023, **30**, 71048–71062.
74 S. J. Malode, M. M. Shanbhag, R. Kumari, D. S. Dkhar, P. Chandra and N. P. Shetti, *J. Pharm. Biomed. Anal.*, 2023, **222**, 115102.
75 N. Dhiman, S. Ghosh, Y. K. Mishra and K. M. Tripathi, *Mater. Adv.*, 2022, **3**, 3101–3122.
76 J. Kaushik, Gunture, K. M. Tripathi, R. Singh and S. K. Sonkar, *Chemosphere*, 2022, **287**, 132105.
77 G. Capellari, E. Chatzi and S. Mariani, *Sensors*, 2018, **18**, 2174.
78 S. Alokita, V. Rahul, K. Jayakrishna, V. Kar, M. Rajesh, S. Thirumalini and M. Manikandan, Recent advances and trends in structural health monitoring, 2019, pp. 53–73.
79 M. Mishra, P. B. Lourenço and G. V. Ramana, *J. Build. Eng.*, 2022, **48**, 103954.
80 G. Seychal, E. Ramasso, P. Le Moal, G. Bourbon, X. Gabrion and V. Placet, *Composites, Part B*, 2022, **236**, 109787.
81 H. Chen, M. B. Müller, K. J. Gilmore, G. G. Wallace and D. Li, *Adv. Mater.*, 2008, **20**, 3557–3561.
82 P. Avouris, *Nano Lett.*, 2010, **10**, 4285–4294.
83 D. Li and R. B. Kaner, *Science*, 2008, **320**, 1170–1171.
84 S.-M. Choi, S.-H. Jhi and Y.-W. Son, *Nano Lett.*, 2010, **10**, 3486–3489.
85 S. Zhang, L. Wen, H. Wang, K. Zhu and M. Zhang, *J. Mater. Chem. C*, 2018, **6**, 5132–5139.
86 S. Ryu, P. Lee, J. B. Chou, R. Xu, R. Zhao, A. J. Hart and S.-G. Kim, *ACS Nano*, 2015, **9**, 5929–5936.
87 Y. Yu, Y. Luo, A. Guo, L. Yan, Y. Wu, K. Jiang, Q. Li, S. Fan and J. Wang, *Nanoscale*, 2017, **9**, 6716–6723.
88 K. Suzuki, K. Yataka, Y. Okumiya, S. Sakakibara, K. Sako, H. Mimura and Y. Inoue, *ACS Sens.*, 2016, **1**, 817–825.
89 K.-H. Kim, S. K. Hong, S.-H. Ha, L. Li, H. W. Lee and J.-M. Kim, *Mater. Horiz.*, 2020, **7**, 2662–2672.
90 P. Ahuja, S. Akiyama, S. K. Ujjain, R. Kukobat, F. Vallejos-Burgos, R. Futamura, T. Hayashi, M. Kimura, D. Tomanek and K. Kaneko, *J. Mater. Chem. A*, 2019, **7**, 19996–20005.

91 D.-H. Kang, H. Sun, M. Luo, K. Lu, M. Chen, Y. Kim, Y. Jung, X. Gao, S. J. Parluhutan and J. Ge, *Nat. Commun.*, 2021, **12**, 5087.
92 S. Quan, Y. Zhang and W. Chen, *Phys. Chem. Chem. Phys.*, 2022, **24**, 23929–23935.
93 Y. Wang, L. Wang, T. Yang, X. Li, X. Zang, M. Zhu, K. Wang, D. Wu and H. Zhu, *Adv. Funct. Mater.*, 2014, **24**, 4666–4670.
94 J. J. Park, W. J. Hyun, S. C. Mun, Y. T. Park and O. O. Park, *ACS Appl. Mater. Interfaces*, 2015, **7**, 6317–6324.
95 H. Kim, A. A. Abdala and C. W. Macosko, *Macromolecules*, 2010, **43**, 6515–6530.
96 H. J. Salavagione, A. M. Díez-Pascual, E. Lázaro, S. Vera and M. A. Gómez-Fatou, *J. Mater. Chem. A*, 2014, **2**, 14289–14328.
97 J. Meng, J. Song, X. Zhang, J. Wang and S. Li, *Compos. Commun.*, 2023, **42**, 101693.
98 W. Zhang, B. Yin, J. Wang, A. Mohamed and H. Jia, *J. Alloys Compd.*, 2019, **785**, 1001–1008.
99 J.-M. Park, D.-J. Kwon, Z.-J. Wang, J.-J. Kim, K.-W. Jang and K. L. DeVries, *Adhes. Sci. Technol.*, 2014, **28**, 1677–1686.
100 D.-J. Kwon, Z.-J. Wang, J.-Y. Choi, P.-S. Shin, K. L. DeVries and J.-M. Park, *Composites, Part A*, 2015, **72**, 160–166.
101 M.-J. Lim, H. K. Lee, I.-W. Nam and H.-K. Kim, *Compos. Struct.*, 2017, **180**, 741–750.
102 K. Tripathi, F. Vincent, M. Castro and J.-F. Feller, *Nanocomposites*, 2016, **2**, 125–134.
103 S. N. Chowdhury, T. T. Tung, Q. T. H. Ta, M. Castro, J. Feller, S. K. Sonkar and K. M. Tripathi, *New J. Chem.*, 2021, **45**, 3675–3682.
104 M. Zhan, G. Pan, F. Zhou, R. Mi and S. P. Shah, *Cem. Concr. Compos.*, 2020, **108**, 103518.
105 G. Yang, X. Feng, W. Wang, Q. OuYang, L. Liu and Z. Wu, *Composites, Part B*, 2021, **204**, 108494.
106 Y. J. Fan, X. Li, S. Y. Kuang, L. Zhang, Y. H. Chen, L. Liu, K. Zhang, S. W. Ma, F. Liang and T. Wu, *ACS Nano*, 2018, **12**, 9326–9332.
107 K.-Y. Shin, J. S. Lee and J. Jang, *Nano Energy*, 2016, **22**, 95–104.
108 X. X. Zhu, X. S. Meng, S. Y. Kuang, X. Di Wang, C. F. Pan, G. Zhu and Z. L. Wang, *Nano Energy*, 2017, **41**, 387–393.
109 S. Park, H. Kim, M. Vosgueritchian, S. Cheon, H. Kim, J. H. Koo, T. R. Kim, S. Lee, G. Schwartz and H. Chang, *Adv. Mater.*, 2014, **26**, 7324–7332.
110 M. K. Mohammed, A. Al-Nafiey and G. Al-Dahash, *Nano Biomed. Eng.*, 2021, **13**, 27–35.
111 B. C. K. Tee, A. Chortos, R. R. Dunn, G. Schwartz, E. Eason and Z. Bao, *Adv. Funct. Mater.*, 2014, **24**, 5427–5434.
112 L. Pan, A. Chortos, G. Yu, Y. Wang, S. Isaacson, R. Allen, Y. Shi, R. Dauskardt and Z. Bao, *Nat. Commun.*, 2014, **5**, 3002.
113 Y. Ma, Y. Yue, H. Zhang, F. Cheng, W. Zhao, J. Rao, S. Luo, J. Wang, X. Jiang and Z. Liu, *ACS Nano*, 2018, **12**, 3209–3216.
114 J. Wang, M.-F. Lin, S. Park and P. S. Lee, *Mater. Today*, 2018, **21**, 508–526.
115 X. Li, Y. J. Fan, H. Y. Li, J. W. Cao, Y. C. Xiao, Y. Wang, F. Liang, H. L. Wang, Y. Jiang and Z. L. Wang, *ACS Nano*, 2020, **14**, 9605–9612.
116 X. Wang, Y. Tang, S. Cheng, C. Liu, Q. Gao, W. Lian, Y. Yuan, A. Li, C. Li and S. Guan, *ACS Appl. Polym. Mater.*, 2023, **5**, 6022–6033.
117 Z. Luo, X. Li, Q. Li, X. Tian, T. Fan, C. Wang, X. Wu and G. Shen, *Adv. Electron. Mater.*, 2020, **6**, 2000269.
118 M. Lin, Z. Zheng, L. Yang, M. Luo, L. Fu, B. Lin and C. Xu, *Adv. Mater.*, 2022, **34**, 2107309.
119 Y. Lu, Y. Yue, Q. Ding, C. Mei, X. Xu, Q. Wu, H. Xiao and J. Han, *ACS Appl. Mater. Interfaces*, 2021, **13**, 50281–50297.
120 C. Wang, K. Xia, H. Wang, X. Liang, Z. Yin and Y. Zhang, *Adv. Mater.*, 2019, **31**, 1801072.
121 K. S. Raju, G. S. Das and K. M. Tripathi, *RSC Sustainability*, 2023, DOI: **10.1039/D3SU00343D**.
122 V. K. Tripathi, G. S. Das, R. K. Gupta, M. Srivastava and K. M. Tripathi, *RSC Sustainability*, 2023, **1**, 2319–2327.
123 G. S. Das, J. Y. Hwang, J.-H. Jang, K. M. Tripathi and T. Kim, *ACS Appl. Energy Mater.*, 2022, **5**, 6663–6670.
124 J. Kaushik, C. Sharma, N. K. Lamba, P. Sharma, G. S. Das, K. M. Tripathi, R. K. Joshi and S. K. Sonkar, *Langmuir*, 2023, **39**, 12865–12877.
125 K. M. Tripathi, T. Kim, D. Losic and T. T. Tung, *Carbon*, 2016, **110**, 97–129.
126 A. Sharma, N. Sharma, A. Kumari, H.-J. Lee, T. Kim and K. M. Tripathi, *Appl. Mater. Today*, 2020, **18**, 100467.
127 J. Hu, J. Yu, Y. Li, X. Liao, X. Yan and L. Li, *Nanomaterials*, 2020, **10**, 664.
128 Y. Li, W. Tong, J. Yang, Z. Wang, D. Wang, Q. An and Y. Zhang, *Chem. Eng. J.*, 2023, **457**, 141356.
129 X. Tang, J. Pionteck and P. Pötschke, *Polymer*, 2023, **268**, 125702.
130 G. S. Das, S. Sarkar, R. Aggarwal, S. K. Sonkar, J.-W. Park, K. M. Tripathi and T. Kim, *Carbon Lett.*, 2019, **29**, 595–603.
131 Y. He, L. Zhao, J. Zhang, L. Liu, H. Liu and L. Liu, *Compos. Sci. Technol.*, 2020, **200**, 108419.
132 D. Jang, H. N. Yoon, I. W. Nam and H. K. Lee, *Compos. Struct.*, 2020, **244**, 112260.
133 S. Jung, P. Thi Huong, S. Sahani, K. M. Tripathi, B. J. Park, Y. H. Han and T. Kim, *J. Electrochem. Soc.*, 2022, **169**, 010509.
134 D. Saini, S. Dumra, V. Kumar, R. Aggarwal, A. R. Naziruddin and S. K. Sonkar, *ACS Appl. Nano Mater.*, 2023, **6**, 1573–1581.
135 L. Peponi, D. Puglia, L. Torre, L. Valentini and J. M. Kenny, *Mater. Sci. Eng., R*, 2014, **85**, 1–46.
136 P. Costa, J. Nunes-Pereira, J. Oliveira, J. Silva, J. A. Moreira, S. Carabineiro, J. Buijnsters and S. Lanceros-Mendez, *Compos. Sci. Technol.*, 2017, **153**, 241–252.
137 B. Gonçalves, J. Oliveira, P. Costa, V. Correia, P. Martins, G. Botelho and S. Lanceros-Mendez, *Composites, Part B*, 2017, **112**, 344–352.

138 B. F. Gonçalves, P. Costa, J. Oliveira, S. Ribeiro, V. Correia, G. Botelho and S. Lanceros-Mendez, *J. Polym. Sci., Part B: Polym. Phys.*, 2016, **54**, 2092–2103.
139 H. Zhao and J. Bai, *ACS Appl. Mater. Interfaces*, 2015, **7**, 9652–9659.
140 P. Costa, S. Gonçalves, H. Mora, S. Carabineiro, J. Viana and S. Lanceros-Mendez, *ACS Appl. Mater. Interfaces*, 2019, **11**, 46286–46295.
141 Q. Zheng, J.-h. Lee, X. Shen, X. Chen and J.-K. Kim, *Mater. Today*, 2020, **36**, 158–179.
142 J. Yuan, Q. Li, L. Ding, C. Shi, Q. Wang, Y. Niu and C. Xu, *ACS Omega*, 2022, **7**, 44428–44437.
143 A. S. Kurian, V. B. Mohan and D. Bhattacharyya, *Sens. Actuators, A*, 2018, **282**, 206–214.
144 P. Song, G. Wang and Y. Zhang, *Sens. Actuators, A*, 2021, **323**, 112659.
145 S. Sun, Y. Liu, X. Chang, Y. Jiang, D. Wang, C. Tang, S. He, M. Wang, L. Guo and Y. Gao, *J. Mater. Chem. C*, 2020, **8**, 2074–2085.
146 M. Cao, S. Fan, H. Qiu, D. Su, L. Li and J. Su, *ACS Appl. Mater. Interfaces*, 2020, **12**, 36540–36547.
147 L. Ma, X. Lei, X. Guo, L. Wang, S. Li, T. Shu, G. J. Cheng and F. Liu, *ACS Appl. Nano Mater.*, 2022, **5**, 7142–7149.
148 M. Wegener, W. Wirges and R. Gerhard-Multhaupt, *Adv. Eng. Mater.*, 2005, **7**, 1128–1131.
149 P. Zhao, S. Wang, A. Kadlec, Z. Li and X. Wang, *Ceram. Int.*, 2016, **42**, 15030–15034.
150 J.-W. Li, C.-Y. Huang, K.-Y. Chen, J.-X. Chen, X.-Y. Hsu, Y.-F. Chen, C.-F. J. Kuo, C.-C. Cheng, M.-C. Suen and C.-W. Chiu, *Polymers*, 2020, **12**, 2999.
151 M. I. Ali Umar, C. C. Yap, R. Awang, M. H. Hj Jumali, M. Mat Salleh and M. Yahaya, *J. Mater. Sci.: Mater. Electron.*, 2013, **24**, 1282–1286.
152 Z. Lou, S. Chen, L. Wang, K. Jiang and G. Shen, *Nano Energy*, 2016, **23**, 7–14.
153 Z. Chen, Z. Wang, X. Li, Y. Lin, N. Luo, M. Long, N. Zhao and J.-B. Xu, *ACS Nano*, 2017, **11**, 4507–4513.
154 Y. Wan, Y. Wang and C. F. Guo, *Mater. Today Phys.*, 2017, **1**, 61–73.
155 T. Huang, S. Yang, P. He, J. Sun, S. Zhang, D. Li, Y. Meng, J. Zhou, H. Tang and J. Liang, *ACS Appl. Mater. Interfaces*, 2018, **10**, 30732–30740.
156 Y. Li, W. Chen and L. Lu, *ACS Appl. Bio Mater.*, 2020, **4**, 122–139.
157 M. Šiškins, M. Lee, D. Wehenkel, R. van Rijn, T. W. de Jong, J. R. Renshof, B. C. Hopman, W. S. Peters, D. Davidovikj and H. S. van der Zant, *Microsyst. Nanoeng.*, 2020, **6**, 102.
158 X. Yang, Y. Wang and X. Qing, *Sens. Actuators, A*, 2019, **299**, 111579.
159 F. Liu, S. Dai, J. Cao, Z. Zhang, G. Cheng and J. Ding, *Sens. Actuators, A*, 2022, **343**, 113672.
160 K. Ke, M. McMaster, W. Christopherson, K. D. Singer and I. Manas-Zloczower, *Composites, Part A*, 2019, **126**, 105614.
161 Z. L. Wang, *ACS Nano*, 2013, **7**, 9533–9557.
162 M. Ha, J. Park, Y. Lee and H. Ko, *ACS Nano*, 2015, **9**, 3421–3427.
163 S.-Y. Xia, Y. Long, Z. Huang, Y. Zi, L.-Q. Tao, C.-H. Li, H. Sun and J. Li, *Nano Energy*, 2022, **96**, 107099.
164 G. M. Rani, C.-M. Wu, K. G. Motora, R. Umapathi and C. R. M. Jose, *Nano Energy*, 2023, **108**, 108211.
165 Y. Lee, J. Kim, B. Jang, S. Kim, B. K. Sharma, J.-H. Kim and J.-H. Ahn, *Nano Energy*, 2019, **62**, 259–267.
166 C.-R. Yang, C.-T. Ko, S.-F. Chang and M.-J. Huang, *Nano Energy*, 2022, **92**, 106791.
167 C. Cooper, R. Young and M. Halsall, *Composites, Part A*, 2001, **32**, 401–411.
168 M. Lucas and R. Young, *Phys. Rev. B: Condens. Matter Mater. Phys.*, 2004, **69**, 085405.
169 W. Qiu, Q. Li, Z.-K. Lei, Q.-H. Qin, W.-L. Deng and Y.-L. Kang, *Carbon*, 2013, **53**, 161–168.
170 N. Kalashnyk, E. Faulques, J. Schjødt-Thomsen, L. R. Jensen, J. C. M. Rauhe and R. Pyrz, *Carbon*, 2016, **109**, 124–130.
171 K. Tsirka, L. Tzounis, A. Avgeropoulos, M. Liebscher, V. Mechtcherine and A. S. Paipetis, *Compos. Sci. Technol.*, 2018, **165**, 240–249.
172 A. P. A. Raju, A. Lewis, B. Derby, R. J. Young, I. A. Kinloch, R. Zan and K. S. Novoselov, *Adv. Funct. Mater.*, 2014, **24**, 2865–2874.
173 G. Tsoukleri, J. Parthenios, K. Papagelis, R. Jalil, A. C. Ferrari, A. K. Geim, K. S. Novoselov and C. Galiotis, *Small*, 2009, **5**, 2397–2402.
174 J. Chu, A. J. Marsden, R. J. Young and M. A. Bissett, *ACS Appl. Mater. Interfaces*, 2019, **11**, 31338–31345.
175 M.-Z. Li, S.-T. Han and Y. Zhou, *Adv. Intell. Syst.*, 2020, **2**, 2000113.
176 M. Zhao, Y. Chen, K. Wang, Z. Zhang, J. K. Streit, J. A. Fagan, J. Tang, M. Zheng, C. Yang and Z. Zhu, *Science*, 2020, **368**, 878–881.
177 S. Wu, Y. Liu, Y. Tang, X. Jiang, L. Liu, X. Liu, J. Cao and Y. Liu, *Nanotechnology*, 2023, **34**, 315501.
178 G. Cheng, H. Xu, N. Gao, M. Zhang, H. Gao, B. Sun, M. Gu, L. Yu, Y. Lin and X. Liu, *Carbon*, 2023, **204**, 456–464.
179 K. Tamersit, *J. Comput. Chem.*, 2019, **18**, 846–855.
180 N. Yogeswaran, E. S. Hosseini and R. Dahiya, *ACS Appl. Mater. Interfaces*, 2020, **12**, 54035–54040.
181 E. Piccinini, G. E. Fenoy, A. L. Cantillo, J. A. Allegretto, J. Scotto, J. M. Piccinini, W. A. Marmisollé and O. Azzaroni, *Adv. Mater. Interfaces*, 2022, **9**, 2102526.
182 J. Liu, S. Bao and X. Wang, *Micromachines*, 2022, **13**, 184.
183 K. Tamersit, M. Kotti and M. Fakhfakh, *Int. J. Electron. Commun.*, 2020, **124**, 153346.
184 P. Miao, J. Wang, C. Zhang, M. Sun, S. Cheng and H. Liu, *Nano-Micro Lett.*, 2019, **11**, 1–37.
185 C. Wang, K. Xia, H. Wang, X. Liang, Z. Yin and Y. Zhang, *Adv. Mater.*, 2019, **31**, 1801072.
186 Y. Ren, Z. Liu, G. Jin, M. Yang, Y. Shao, W. Li, Y. Wu, L. Liu and F. Yan, *Adv. Mater.*, 2021, **33**, 2008486.

187 V. Amoli, J. S. Kim, S. Y. Kim, J. Koo, Y. S. Chung, H. Choi and D. H. Kim, *Adv. Funct. Mater.*, 2020, **30**, 1904532.
188 M. Mehrali, S. Bagherifard, M. Akbari, A. Thakur, B. Mirani, M. Mehrali, M. Hasany, G. Orive, P. Das and J. Emneus, *Adv. Sci.*, 2018, **5**, 1700931.
189 K. Liu, Y. Jiang, Z. Bao and X. Yan, *CCS Chem.*, 2019, **1**, 431–447.
190 D. C. Kim, H. J. Shim, W. Lee, J. H. Koo and D. H. Kim, *Adv. Mater.*, 2020, **32**, 1902743.
191 P. Miao, J. Wang, C. Zhang, M. Sun, S. Cheng and H. Liu, *Nano-Micro Lett.*, 2019, **11**, 1–37.
192 L. Miao, J. Wan, Y. Song, H. Guo, H. Chen, X. Cheng and H. Zhang, *ACS Appl. Mater. Interfaces*, 2019, **11**, 39219–39227.
193 C. Mu, Y. Song, W. Huang, A. Ran, R. Sun, W. Xie and H. Zhang, *Adv. Funct. Mater.*, 2018, **28**, 1707503.
194 C. Yang, A. Abodurexiti and X. Maimaitiyiming, *Macromol. Mater. Eng.*, 2020, **305**, 2000287.
195 S. Harada, W. Honda, T. Arie, S. Akita and K. Takei, *ACS Nano*, 2014, **8**, 3921–3927.
196 L. Chen, M. Weng, P. Zhou, F. Huang, C. Liu, S. Fan and W. Zhang, *Adv. Funct. Mater.*, 2019, **29**, 1806057.
197 S. G. Yoon and S. T. Chang, *J. Mater. Chem. C*, 2017, **5**, 1910–1919.
198 D. H. Ho, Q. Sun, S. Y. Kim, J. T. Han, D. H. Kim and J. H. Cho, *Adv. Mater.*, 2016, **28**, 2601–2608.
199 H. Xu, J. X. Xiang, Y. F. Lu, M. K. Zhang, J. J. Li, B. B. Gao, Y. J. Zhao and Z. Z. Gu, *ACS Appl. Mater. Interfaces*, 2018, **10**, 11785–11793.
200 H. Liu, H. Xiang, Y. Wang, Z. Li, L. Qian, P. Li, Y. Ma, H. Zhou and W. Huang, *ACS Appl. Mater. Interfaces*, 2019, **11**, 40613–40619.
201 H. Niu, W. Yue, Y. Li, F. Yin, S. Gao, C. Zhang, H. Kan, Z. Yao, C. Jiang and C. Wang, *Sens. Actuators, B*, 2021, **334**, 129637.
202 J. Luo, Y. Yao, X. Duan and T. Liu, *J. Mater. Chem. C*, 2018, **6**, 4727–4736.
203 X. Wang, O. Yue, X. Liu, M. Hou and M. Zheng, *J. Chem. Eng.*, 2020, **392**, 123672.
204 A. Krishnamoorthy, S. Chandrapalan, S. Bosch, A. Bannaga, N. K. De Boer, T. G. De Meij, M. Leja, G. B. Hanna, N. De Vietro and D. Altomare, *Sensors*, 2023, **23**, 1377.
205 Y. Fu, H. He, Y. Liu, Q. Wang, L. Xing and X. Xue, *J. Mater. Chem. C*, 2017, **5**, 1231–1239.
206 E. Davoodi, H. Montazerian, R. Haghniaz, A. Rashidi, S. Ahadian, A. Sheikhi, J. Chen, A. Khademhosseini, A. S. Milani and M. Hoorfar, *ACS Nano*, 2020, **14**, 1520–1532.
207 S. Y. Kim, S. Park, H. W. Park, D. H. Park, Y. Jeong and D. H. Kim, *Adv. Mater.*, 2015, **27**, 4178–4185.
208 D. Saini, Gunture, J. Kaushik, R. Aggarwal, K. M. Tripathi and S. K. Sonkar, *ACS Appl. Nano Mater.*, 2021, **4**, 12825–12844.
209 J. Zhang, M. Wang, Z. Yang and X. Zhang, *Carbon*, 2021, **176**, 139–147.
210 C. Xu, H. Lu, Z. Liu, N. Luo and A. Wei, *J. Mater. Sci.: Mater. Electron.*, 2023, **34**, 906.
211 S. Li, R. Xu, J. Wang, Y. Yang, Q. Fu and C. Pan, *J. Colloid Interface Sci.*, 2022, **617**, 372–382.
212 Y.-J. Kim, J. Y. Cha, H. Ham, H. Huh, D.-S. So and I. Kang, *Curr. Appl. Phys.*, 2011, **11**, S350–S352.
213 Z. Liu, G. Wang, W. Pei, C. Wei, X. Wu, Z. Dou, Y. Li, Y. Wang and H. Chen, *J. Mater. Chem. B*, 2020, **8**, 8794–8802.
214 Z. Pei, Q. Zhang, K. Yang, Z. Yuan, W. Zhang and S. Sang, *Adv. Mater. Technol.*, 2021, **6**, 2100038.
215 S. Wang, H. Ning, N. Hu, Y. Liu, F. Liu, R. Zou, K. Huang, X. Wu, S. Weng and Alamusi, *Adv. Mater. Interfaces*, 2020, **7**, 1901507.
216 H. Tian, Y. Shu, X.-F. Wang, M. A. Mohammad, Z. Bie, Q.-Y. Xie, C. Li, W.-T. Mi, Y. Yang and T.-L. Ren, *Sci. Rep.*, 2015, **5**, 8603.
217 G. Y. Bae, S. W. Pak, D. Kim, G. Lee, D. H. Kim, Y. Chung and K. Cho, *Adv. Mater.*, 2016, **28**, 5300–5306.
218 Y. Wei, S. Chen, X. Dong, Y. Lin and L. Liu, *Carbon*, 2017, **113**, 395–403.
219 W. Liu, Q. Chen, Y. Huang, D. Wang, L. Li and Z. Liu, *Carbon*, 2022, **190**, 245–254.
220 A. Qiu, M. Aakyiir, R. Wang, Z. Yang, A. Umer, I. Lee, H.-Y. Hsu and J. Ma, *Sci. Rep.*, 2020, **1**, 235–243.
221 F. S. Irani, A. H. Shafaghi, M. C. Tasdelen, T. Delipinar, C. E. Kaya, G. G. Yapici and M. K. Yapici, *Micromachines*, 2022, **13**, 119.
222 X. W. Zhang, Y. Pan, Q. Zheng and X. S. Yi, *J. Polym. Sci., Part B: Polym. Phys.*, 2000, **38**, 2739–2749.
223 S. Wang, F. Lenzini, D. Chen, P. Tanner, J. Han, D. Thiel, M. Lobino and Q. Li, *J. Mater. Sci. Technol.*, 2023, **141**, 110–115.
224 A. del Bosque, X. F. Sánchez-Romate, M. Sanchez and A. Urena, *Carbon*, 2022, **192**, 234–248.
225 A. del Bosque, X. F. Sánchez-Romate, A. Gómez, M. Sánchez and A. Ureña, *Sens. Actuators, A*, 2023, **353**, 114249.
226 H. Yang, L. Yuan, X. Yao and D. Fang, *J. Mech. Phys. Solids*, 2020, **139**, 103943.
227 R. Nazar, U. Mehmood, H. Ahmed, A. Imran and S. A. Raza, *Polym. Corros. Inhib. Greening Chem. Petrochem. Ind.*, 2022, 331–352.
228 J. Su, W. Liu, S. Chen, W. Deng, Y. Dou, Z. Zhao, J. Li, Z. Li, H. Yin, X. Ding and S. Song, *ACS Sens.*, 2020, 3979–3987.
229 Y. Li, C. Zheng, S. Liu, L. Huang, T. Fang, J. X. Li, F. Xu and F. Li, *ACS Appl. Mater. Interfaces*, 2020, **12**(21), 23764–23773.
230 B. Taherkhani, S. Rahmani and O. Atalay, *J. Mater.: Des. Appl.*, 2023, **237**(10), DOI: **10.1177/14644207231174325**.